

## Intense explosive activity in the early Holocene at Pico de Orizaba volcano: Revisiting the Xilomich eruptive episode

Delphine Sourisseau <sup>a,\*</sup>, José Luis Arce <sup>b</sup>, José Luis Macías <sup>c</sup>, Laura E. Beramendi-Orosco <sup>d</sup>, José Juan Carrillo-Mondragón <sup>e</sup>, Galia González-Hernández <sup>f</sup>

<sup>a</sup> Postdoctoral Fellow SECIHTI - Instituto de Geología, Universidad Nacional Autónoma de México, C.U. Coyoacán, 04510 Ciudad de México, Mexico

<sup>b</sup> Instituto de Geología, Universidad Nacional Autónoma de México, C.U. Coyoacán, 04510 Ciudad de México, Mexico

<sup>c</sup> Instituto de Geofísica, Universidad Nacional Autónoma de México, C.U. Coyoacán, 04510 Ciudad de México, Mexico

<sup>d</sup> Laboratorio Universitario de Radiocarbono, Instituto de Geología, Universidad Nacional Autónoma de México, C.U., 04510 Ciudad de México, Mexico

<sup>e</sup> Posgrado en Ciencias de la Tierra, Universidad Nacional Autónoma de México, C.U. Coyoacán, 04510 Ciudad de México, Mexico

<sup>f</sup> Laboratorio Universitario de Radiocarbono, Instituto de Geofísica, Universidad Nacional Autónoma de México, C.U., 04510 Ciudad de México, Mexico

### ARTICLE INFO

#### Keywords:

Dome growth and collapse  
Vulcanian eruption  
PDC deposits  
Holocene activity  
Radiometric dating  
Pico de Orizaba volcano

### ABSTRACT

Pico de Orizaba is a Pleistocene to Holocene stratovolcano located in the easternmost part of the Trans-Mexican Volcanic Belt. Repeated cycles of dome growth and collapse, along with Vulcanian to Plinian explosive activity, have occurred during the past 650 ka. These eruptions have produced a complex sequence of scoria-and-ash, pumice-and-ash, block-and-ash flows and pumice fallout, interbedded with andesitic to dacitic lava flows that constitute the modern volcanic edifice (Citlaltépetl volcano). Based on detailed field descriptions, stratigraphic correlations, grain size and componentry analyses, and five new <sup>14</sup>C radiocarbon ages, we reconstruct the eruptive history of the Xilomich eruptive episode deposited south of Pico de Orizaba. Our results indicate that at least ten pyroclastic flows were emplaced during the Xilomich eruptive episode between 8980 and 8170 years BP. These deposits record the occurrence of at least four Vulcanian eruptions and two dome-destruction events, which generated scoria-and-ash and block-and-ash pyroclastic flows. Pyroclastic flows generated by eruptions comparable to the Xilomich episode could extend as far as populated areas like Maltrata, Ciudad Mendoza, and Orizaba, located within a 30-km radius, posing a potential threat to approximately 310,500 inhabitants south of Pico de Orizaba.

### 1. Introduction

Explosive eruptions at andesitic stratovolcanoes are driven by the interplay of viscous magma ascent, gas pressurization beneath lava domes, and the periodic obstruction and reopening of volcanic conduits (Clarke et al., 2002; Cashman and Sparks, 2013). These processes lead to highly unstable conditions within the volcanic edifice, resulting in intermittent explosive activity. Two common eruptive behaviors in these systems are Vulcanian eruptions and the collapse of domes, both of which generate pyroclastic density currents, posing substantial hazards to nearby populations. Vulcanian eruptions involve short-lived, violent explosions caused by rapid decompression of pressurized gases and magma trapped beneath a solidified lava dome or conduit plug (Clarke et al., 2002; Druitt et al., 2002). These eruptions produce scoria-and-ash flows accompanied by tephra fallout. Partial or total collapse of lava

domes generates dense block-and-ash flows composed of hot, angular dome fragments mixed with volcanic ash. Such events have been extensively documented in several volcanoes as Colima (Saucedo et al., 2005; Varley et al., 2010), Mount Unzen (Yamamoto et al., 1993), Soufrière Hills (Cole et al., 2002), and Merapi (Kelfoun et al., 2021). Understanding the frequency, dynamics, and deposits associated with these eruption styles is essential for accurate volcanic hazard assessments and effective risk mitigation strategies.

Pico de Orizaba is a large andesitic to dacitic stratovolcano that exhibits eruptive behavior similar to other intermediate-composition volcanoes such as Soufrière Hills and Mount Unzen (Cole et al., 2024; Nakada and Fujii, 1993). Active from the Middle Pleistocene to the Holocene, this volcano is located within a densely populated region, with more than 500,000 inhabitants living within a 40 km radius (National Institute of Statistics and Geography, <https://en.www.inegi.org>.

\* Corresponding author.

E-mail address: [d.sourisseau@geologia.unam.mx](mailto:d.sourisseau@geologia.unam.mx) (D. Sourisseau).

mx.; Carrasco-Núñez, 2000) (Fig. 1). Its stratigraphic record documents a complex eruptive history characterized by alternating effusive and explosive activity, including episodes of lava dome growth and collapse, Vulcanian and Plinian eruptions, and flank collapse events. These eruptive processes have produced diverse volcanic deposits, including block-and-ash flows, scoria-and-ash flows, pumice fallout, and interbedded andesitic to dacitic lava flows (Cantagrel et al., 1984; Höskuldsson and Robin, 1993; Carrasco-Núñez and Rose, 1995; Rossotti and Nuñez, 2004).

Officially classified as an active but currently dormant volcano, Pico de Orizaba continues to show signs of activity, notably fumarolic emissions at its summit reported by residents (Secretaría de Seguridad y Protección Ciudadana, Coordinación Nacional de Protección Civil, and CENAPRED, 2022). Given its eruptive potential and proximity to population centers, new studies on its eruptive history and reassessments of its Holocene record (e.g., Vásquez-Montoya et al., 2025) are necessary to improve the volcanic hazard assessment and support future risk mitigation strategies and land-use planning. The Xilomich eruptive episode of Pico de Orizaba volcano (8–9 ka) was marked by intense explosive

activity (Carrasco-Núñez and Rose, 1995; Rossotti and Nuñez, 2004). Yet, previous studies provide limited stratigraphic and chronological constraints for the southern sector of Pico de Orizaba (Fig. 9).

In this study, we present a detailed reconstruction of the pyroclastic sequence deposited on the southern flanks of Pico de Orizaba during the Xilomich eruptive episode (Höskuldsson and Robin, 1993). Using field observations, stratigraphic correlations, grain size and component analyses, petrographic descriptions, and five new radiocarbon dates from pyroclastic flow deposits, we reconstruct the eruptive chronology and characterize the volcanic processes responsible for the emplacement of these deposits. We provide petrographic and componentry data for each pyroclastic flow unit, combined with radiocarbon dating, which are essential for future stratigraphic correlations.

## 2. Geological background

Pico de Orizaba volcano is located in the easternmost sector of the Trans-Mexican Volcanic Belt (TMVB) (Fig. 1). The TMVB is a continental volcanic arc of Middle Miocene to Holocene age, formed by the

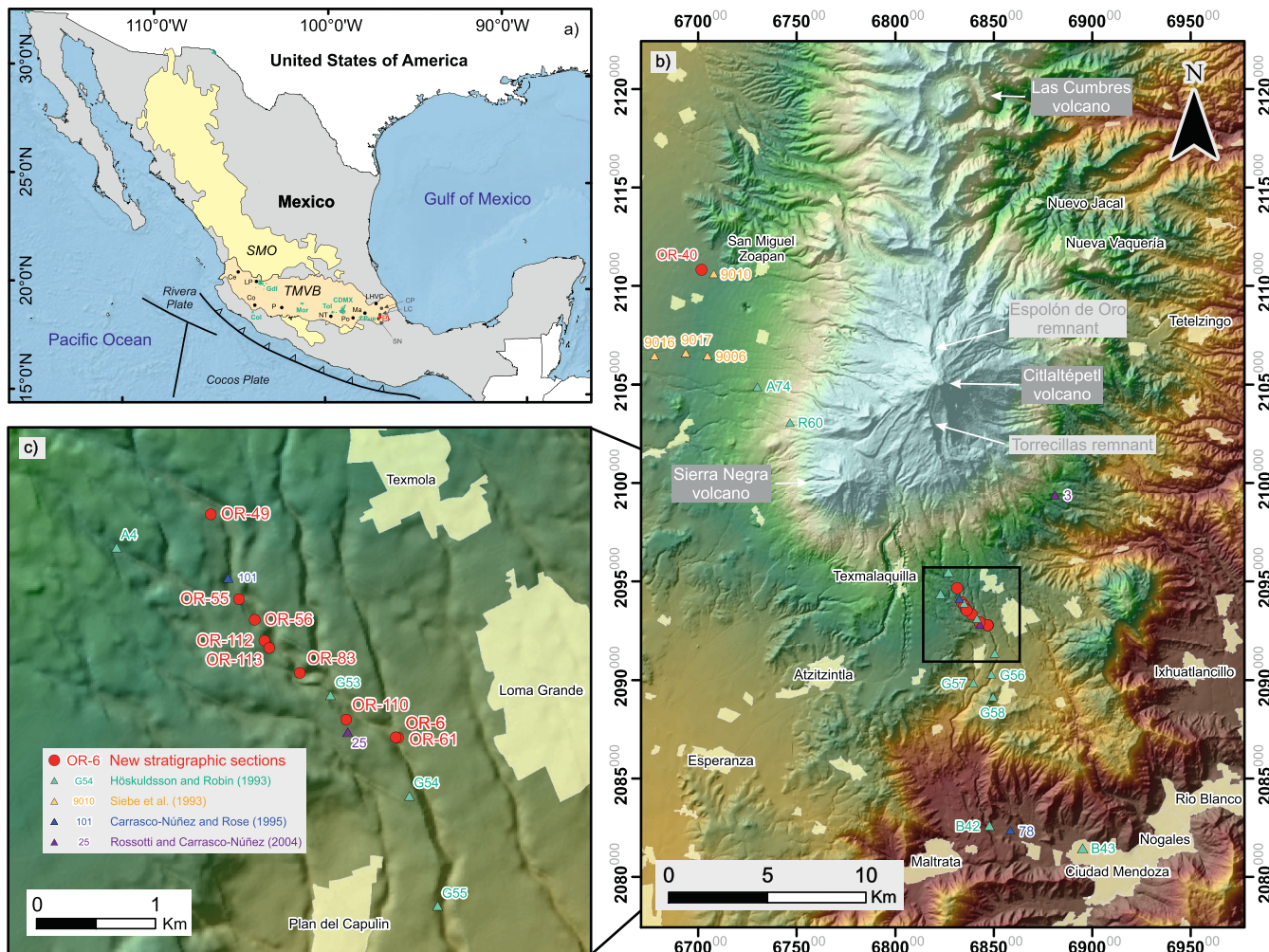


**Fig. 1.** a) Location map of Pico de Orizaba (red-filled circle) at the southern end of the Citlaltépetl–Cofre de Perote Volcanic Range (CCPVR) within the easternmost part of the Trans-Mexican Volcanic Belt (TMVB); and adjacent volcanoes of the CCPVR, Sierra Negra (SN), Las Cumbres (LC), and Cofre de Perote (CP). Other volcanic centers of the TMVB are Ce = Ceboruco; Co = Colima; LP = La Primavera; P = Parícutin; NT = Nevado de Toluca; Po = Popocatépetl; Ma = Malinche; and LHVC = Los Humeros. The largest cities are represented in green. b and c) Shaded relief model of the Pico de Orizaba and Sierra Negra volcanoes. The modern Pico de Orizaba volcano (Citlaltépetl) was built on the remnants of the Torrecillas and Espolón de Oro edifices. The map shows the stratigraphic sections described in this study (coordinates in Supplementary Material Table 1), along with selected sections from previous studies, including those of Höskuldsson and Robin (1993; coordinates georeferenced from their Fig. 6 using ArcGIS), Siebe et al. (1993), Carrasco-Núñez and Rose (1995), and Rossotti and Nuñez (2004). The map uses the World Geodetic System 1984 (WGS 84) ellipsoid in the UTM Zone 14 coordinate system at a 1:100,000 scale. (2-column fitting image). (For interpretation of the references to color in this figure legend, the reader is referred to the web version of this article.)

subduction of the Rivera and Cocos plates beneath the North American plate along the Middle America Trench (Nixon, 1982; DeMets and Stein, 1990; Pardo and Suárez, 1995; Ferrari et al., 2012). Volcanism in the easternmost portion of the TMVB is attributed to the oblique subduction of the Cocos plate beneath the North American plate (Höskuldsson and Robin, 1993) (Fig. 1). Friction between the Cocos and North America plates in the underlying Pico de Orizaba basement has been proposed to facilitate magma ascent through a fractured continental crust associated with a sinistral transform fault system (Mooser and Maldonado Koerdell, 1961; Höskuldsson, 1992).

Pico de Orizaba is bordered to the west by the Serdán-Oriental Basin (SOB; Cavazos-Alvarez et al., 2024) and to the northwest by the Los Humeros Volcanic Complex (LHVC; Carrasco-Núñez et al., 2018) (Fig. 1). The volcano overlies a regional basement composed of Cretaceous limestone and shale, forming a NW-SE trending folded and faulted mountain belt (Yáñez and García, 1982). This sedimentary sequence is partially covered by Quaternary calc-alkaline volcanic rocks of the TMVB (Carrasco-Núñez et al., 2006).

Pico de Orizaba coexists with the Cofre de Perote, La Gloria Complex, Las Cumbres, and Sierra Negra volcanoes along the 70-km-long, north-south-trending Citlaltépetl - Cofre de Perote volcanic range (CCPVR). These volcanic structures exhibit a progressive southward decrease in age from Cofre de Perote to Pico de Orizaba (Höskuldsson and Robin, 1993). Cofre de Perote, at the northern end of the CCPVR, is a 4282 m-high andesitic stratovolcano active between 1.3 and 0.24 Ma, marked by a summit collapse structure (Robin and Cantagrel, 1982; Carrasco-Núñez et al., 2010, 2021). Further south, Las Cumbres is a 3940 m-high andesitic volcano dated at  $365 \pm 15$  ka (Rodríguez, 2005), distinguished by a 3.5 km-wide circular structure with a central summit dome (Carrasco-Núñez, 2000). Pico de Orizaba, the youngest and most prominent volcano (highest peak in Mexico, 5685 m above sea level), is an andesitic to dacitic stratovolcano that formed between 650 ka and the present (Höskuldsson, 1992). Sierra Negra volcano (4580 masl) is located approximately 7 km southwest of Pico de Orizaba, and it is believed to have been active contemporaneously with Pico de Orizaba (Carrasco-Núñez, 2000).

Carrasco-Núñez (2000) proposed a three-phase evolution model to describe the formation of the Pico de Orizaba volcano: (Phase I) construction and destruction of the Torrecillas volcano; (Phase II) construction and destruction of the Espolón de Oro volcano; and (Phase III) construction of the current Citlaltépetl stratovolcano.

Torrecillas (650–210 ka): The initial phase corresponds to the construction of the Torrecillas volcano during the Middle Pleistocene, around 650 ka (Cantagrel and Robin, 1979; Höskuldsson, 1992). Volcanic activity during this phase was predominantly effusive, producing basaltic-andesite to andesite lava flows. Phase I concluded between 290 and 210 ka with the collapse of the Torrecillas edifice, which generated the Jamapa debris avalanche. This avalanche flowed along the Jamapa River on the northeastern flank of the volcano, extending as far as 75 km from the summit (Carrasco-Núñez and Rose, 1995; Carrasco-Núñez, 2000). A remnant of the Torrecillas edifice is still exposed south of the present-day volcano (Fig. 1b).

Espolón de Oro (210–16.5 ka): This phase marks the construction of the Espolón de Oro volcano on the remnants of the Torrecillas edifice around 210 ka (Carrasco-Núñez, 2000). Volcanic activity during this stage was dominated by the effusion of andesitic to dacitic lava flows. Around 16.5 ka, the collapse of the Espolón de Oro edifice (M. Sheridan, unpublished data) generated the 2 km<sup>3</sup> Tetelzingo debris avalanche (Carrasco-Núñez et al., 1993). The avalanche descended the eastern flank of the volcano, traveling approximately 13 km from the summit to the present-day location of the town of Tetelzingo. A remnant of the Espolón de Oro volcano is still observed north of the present-day edifice (Fig. 1b).

Citlaltépetl (13 ka – Present): This phase corresponds to the construction of the modern Citlaltépetl volcano on the remnants of the

Espolón de Oro edifice around 13 ka (Robin and Cantagrel, 1982). It was marked by intense effusive and explosive activity that produced a sequence of dacitic lava flows interlayered with andesitic to dacitic pyroclastic flow and fallout deposits.

The eruptive history of Citlaltépetl has been classified into nine eruptive episodes by Höskuldsson and Robin (1993): Chocaman (12,900 yr BP), Tlachichuca (10,600 yr BP), Coscomatepec (9400 yr BP), Xilomich (8710–8170 yr BP), Loma Grande (7020–6200 yr BP), Avalos (4660–4060 yr BP), El Jacal (3450–3400 yr BP), Texmola (1910–1810 yr BP), and Excola (690 yr BP).

These authors described the Xilomich eruptive episode as a sequence of four scoria-and-ash and block-and-ash pyroclastic flow deposits, dated between 8710 and 8170 yr BP (Höskuldsson and Robin, 1993). The deposits were later overlain by a plinian pumice fallout, designated as T-II. A scoria-and-ash flow deposit described west of Pico de Orizaba was dated at 8710 yr BP, marking the onset of the episode, while a block-and-ash flow emplaced to the south of the volcano and dated at 8170 yr BP was interpreted to represent its final stage (Höskuldsson and Robin, 1993). This eruptive episode was notable for its widespread dispersion, with pyroclastic flows deposited in all directions around Pico de Orizaba.

The Xilomich episode was also described by Carrasco-Núñez and Rose (1995) using another nomenclature; they defined this sequence as the “Citlaltépetl Ignimbrite”, subdivided into Lower and Upper members and dated from 8500 to 9000 yr BP. The Lower Member is a scoria-and-ash flow deposit containing degassing pipe structures, overlain by a pumice lens that yielded a radiocarbon age of 8760 yr BP from embedded carbonized logs (Carrasco-Núñez and Rose, 1995). The Upper Member consists of a yellow pyroclastic fall layer, overlain by a pumice-and-ash flow deposit that also displays degassing pipe structures. Large carbonized logs at the base of this deposit provided a radiocarbon age of 8660 yr BP (Carrasco-Núñez and Rose, 1995).

Later, Rossotti and Nuñez (2004) described the “Citlaltépetl Pumice” (that is part of the Xilomich episode) as a sequence of pyroclastic fall deposits designated as Layers A, C, E–F, and H interbedded with the pyroclastic flow deposits of the Citlaltépetl Ignimbrite. These flows, dated between 9475 and 8505 yr BP, were defined as Flow 1/Layer 1, Flow 2/Layer 2, Flow 3/Layer 3, and Flow 4/Layer 4 by Rossotti and Nuñez (2004) and Rossotti et al. (2006). The Layers E–F pyroclastic fall deposits are thought to have been deposited between 8760 and 8660 yr BP (Rossotti and Nuñez, 2004). In contrast, Layer H was identified above a fallout deposit dated at 8505 yr BP (Rossotti and Nuñez, 2004). More recently, Vásquez-Montoya et al. (2025) described two scoria pyroclastic fall deposits, the Lower and Upper Citlaltépetl. The Lower unit overlies a paleosol dated to 8620 yr BP, whereas the Upper unit lies between two paleosols dated to 8270 and 8250 yr BP.

### 3. Materials and methods

#### 3.1. Fieldwork and sampling

More than 50 stratigraphic sections were described south of Pico de Orizaba during field seasons carried out in 2024 and 2025, in the vicinity of the towns of Texmalaquilla, Texmola, Plan del Capulín, and Loma Grande (Fig. 1). From these, nine representative sections were selected to characterize the deposits of the Xilomich eruptive episode. The pyroclastic deposits were characterized based on their internal structure (thickness, geometry, upper and lower boundaries), clast size, grading, and componentry (clast type and mineralogy) in order to reconstruct the eruptive sequence. From the selected sections, we collected six samples for grain size and componentry analyses to characterize the pyroclastic sequence. Charcoal fragments found within the pyroclastic flow deposits were collected to estimate the age of the deposits. The nomenclature used for bed thickness, grain size, and sorting follows the classification of Sohn and Chough (1989).

### 3.2. Grain size and component analysis

Samples from the pyroclastic layers were dry-sieved at  $1\Phi$  intervals between  $-6\Phi$  to  $4\Phi$  at the *Instituto de Geofísica Unidad Michoacán (IGUM)* and the *Instituto de Geofísica (IGF), Universidad Nacional Autónoma de México (UNAM)* in Morelia and Mexico City, respectively. Granulometric statistical parameters ( $M_{dp}$  and  $\sigma_\phi$ ) were calculated for each sample, following [Inman \(1952\)](#) to characterize the grain size of the pyroclastic flow units (Supplementary Material Table 2). Fragments from the  $-6$  to  $1\Phi$  size sieve fractions (i.e., 0.5 to 64 mm) were examined visually and under a binocular microscope to identify component types, including dense rock, scoria, pumice, crystals, and lithic fragments. More than 500 particles were counted per size fraction to estimate the relative abundance of each component, allowing for the identification of changes throughout the stratigraphic sequence (Supplementary Material Tables 3 and 4).

### 3.3. Petrography of the juvenile components

Six samples of scoria, pumice, and poorly vesicular fragments from pyroclastic flow deposits were selected for thin section preparation at the *Instituto de Geología (IGL), UNAM*, Mexico City. The thin sections were analyzed using a Leica DM 2700 P petrographic microscope to characterize the texture and mineralogical phases of the fragments. Modal analyses were manually performed on the thin sections by counting 1000 points at regular intervals of 0.5 mm in both horizontal and vertical directions. The phases identified at each point were categorized into plagioclase, orthopyroxene, clinopyroxene, amphibole, olivine, rock, vesicles, and groundmass (microlites + glass).

### 3.4. Radiocarbon dating

Five radiocarbon dating analyses were performed on carbonized wood fragments collected from pyroclastic flows in the stratigraphic sections OR-6, OR-49, OR-55, OR-56, and OR-61, south of Pico de Orizaba (Figs. 1b-c).

A carbonized wood fragment collected from the base of a scoria-and-ash flow at section OR-61 was sent to the Beta Analytic Radiocarbon Dating Laboratory (Miami, Florida, USA) for  $^{14}\text{C}$  activity measurements via Accelerator Mass Spectrometry (AMS). Details about the procedure and analytical method are available on the laboratory website (<http://www.radiocarbon.com/beta-lab.htm>).

The rest of the charcoal samples were analyzed at the *Laboratorio Universitario de Radiocarbono (LUR)* of the IGL-UNAM. These charcoal fragments were collected from the base of a scoria-and-ash pyroclastic flow at sections OR-6 and OR-55, as well as from pumice lenses at sections OR-49 and OR-56. The  $^{14}\text{C}$  content of each sample was measured using a Wallac Quantulus 1220 ultra-low level liquid scintillation spectrometer (Perkin Elmer). Further methodological information is available in [Beramendi-Orosco et al. \(2006\)](#).

All age calibrations were performed in OxCal version 4.4.4 ([Bronk Ramsey, 2021](#)) using the IntCal20 calibration curve ([Reimer et al., 2020](#)). Modeled calibrated ages are constrained by stratigraphic order and the sampling unit of each charcoal sample.

### 4. Radiocarbon results

Five radiocarbon ages obtained from carbonized wood fragments were used to correlate the pyroclastic deposits across stratigraphic sections and to refine the eruptive history of the Xilomich episode of Pico de Orizaba (Table 1). Detailed results of the radiocarbon dating analyses, including percent Modern Carbon (pMC),  $\Delta^{14}\text{C}$  (‰),  $\delta^{13}\text{C}$  (‰), calibrated ages ( $2\sigma$ , cal BP), and modeled calibrated ages ( $2\sigma$ , cal BP), are provided in the Supplementary Material Table 7.

Carbonized wood fragments collected from the pyroclastic flows yielded conventional radiocarbon ages of  $8890 \pm 90$  yr BP (sample OR-55A),  $8805 \pm 100$  (OR-6C),  $8785 \pm 90$  yr BP (OR-56B),  $8750 \pm 30$  yr BP (OR-61B), and  $8700 \pm 90$  yr BP (OR-49A).

Calibrated ages for these samples are statistically similar,  $10228-9688$  (9985) to  $10121-9530$  (9703) cal BP, indicating emplacement within a short period. However, as observed in the field, the dated charcoal samples come from distinct stratigraphic horizons (Xil-1 to Xil-5; Fig. 3). To improve temporal resolution, we implemented a Bayesian stratigraphic Sequence in OxCal v4.4.4, with radiocarbon samples grouped by pyroclastic unit and ordered according to field stratigraphy. The resulting modeled calibrated ranges are narrower than the unmodeled distributions (“with model” and “without model” in Supplementary Material Table 7), allowing clearer age differentiation across southern-sector deposits.

### 5. Revised stratigraphy of the Xilomich episode

Stratigraphic sections were described along the Encino river, west of the towns of Loma Grande and Texmola, south of Pico de Orizaba (Figs. 1b-c). The description and correlation of the best-preserved stratigraphic sections, supported by grain-size and componentry analyses, as well as five new radiocarbon dates, enabled the identification of a complex pyroclastic sequence composed of scoria-and-ash, pumice-and-ash, and block-and-ash pyroclastic flow deposits interbedded with pyroclastic fall deposits (Fig. 2). The Xilomich sequence rests atop a 30 to 60 cm-thick paleosol marked by a sharp erosional contact (sections OR-6 and OR-55). This paleosol is estimated to have formed throughout approximately 500 to 1000 years (E. Solleiro, pers. comm.; [Targolian and Krasilnikov, 2007](#)). The Xilomich sequence reaches an estimated cumulative thickness of  $\sim 31$  m at a distance of 12.5 km from the volcano summit in the Encino River (section OR-6). Conventional radiocarbon age constrains the emplacement of these deposits between  $8890 \pm 90$  yr BP (this work) and  $8170$  yr BP ([Höskuldsson and Robin, 1993](#)). The observation of paleosol layers, charred grass and tree twig horizons, reworked material, and pyroclastic fall deposits led to the identification of ten pyroclastic layers, designated as Xil-1 through Xil-10, and described below in stratigraphic order from oldest to youngest (Fig. 3).

#### 5.1. Xil-1 pf

This layer is a 4.5-m-thick massive, poorly sorted, gray-pink, scoria-and-ash pyroclastic flow deposit in section OR-6 (Fig. 4c,e,f). The deposit is characterized by black-beige banded scoria and black dense scoria containing abundant beige pumice lenses and/or nodules with some gray angular xenoliths (samples OR-6C and OR-55A). Numerous

**Table 1**

AMS and  $^{14}\text{C}$  radiocarbon ages of carbonized wood fragments collected in pyroclastic flows south of Pico de Orizaba. (1-column fitting table).

Sample name	UTM zone 14Q coordinates		Method	Laboratory Code	Sample type	Chemical pretreatment	Conventional Radiocarbon Age ( $1\sigma$ ) [years BP]
	X	Y					
OR-49A	683,131	2,094,643	$^{14}\text{C}$	UNAM-24209	Carbonized wood	AAA	$8700 \pm 90$
OR-61B	684,683	2,092,765	AMS	Beta-732565	Carbonized wood	AAA	$8750 \pm 30$
OR-56B	683,498	2,093,754	$^{14}\text{C}$	UNAM-24206	Carbonized wood	AAA	$8785 \pm 90$
OR-6C	684,706	2,092,763	$^{14}\text{C}$	UNAM-24176	Carbonized wood	AAA	$8805 \pm 100$
OR-55A	683,366	2,093,929	$^{14}\text{C}$	UNAM-24207	Carbonized wood	AAA	$8890 \pm 90$

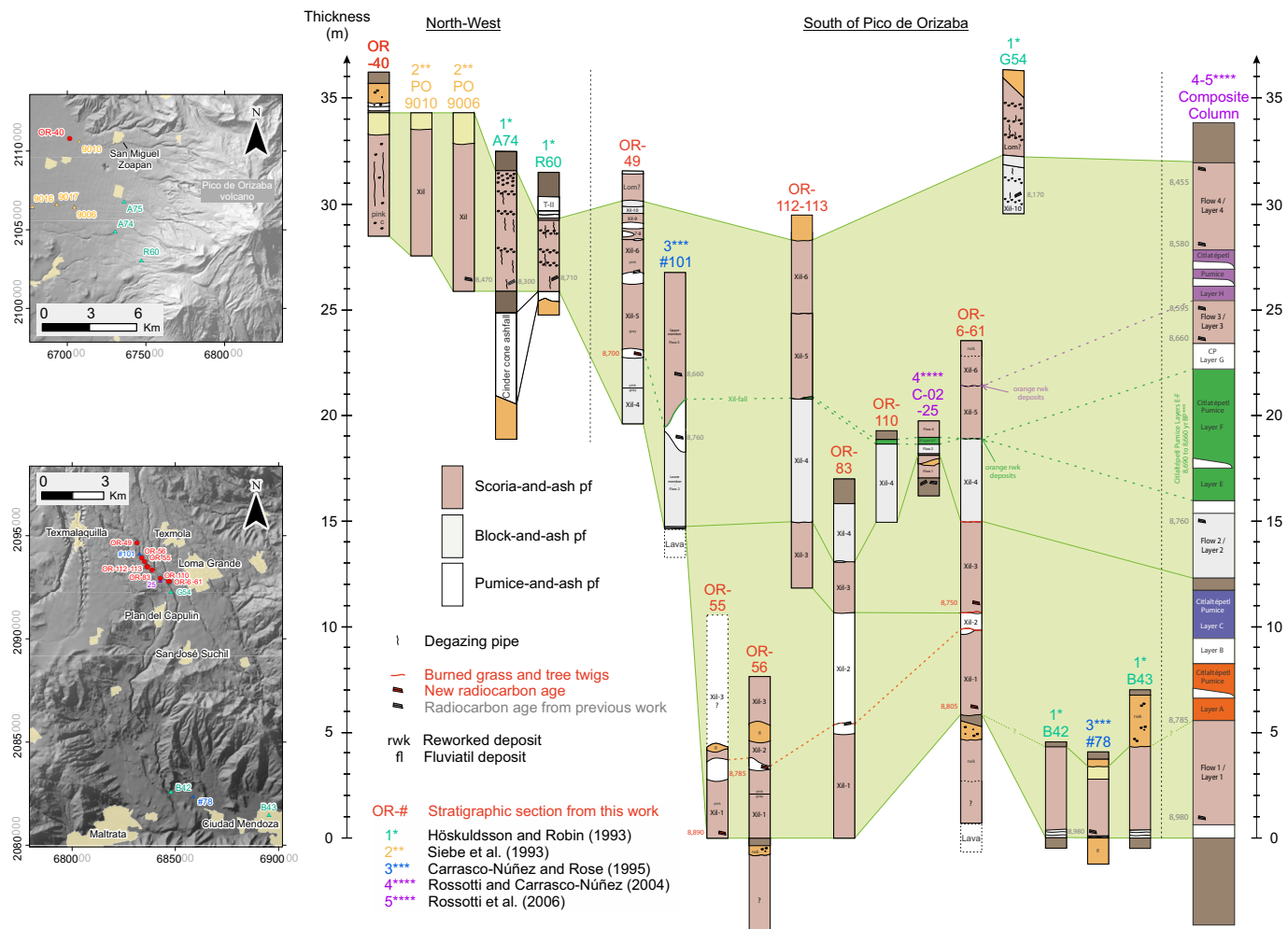


**Fig. 2.** Correlation of the stratigraphic sections described north-west and south of Pico de Orizaba stratovolcano, along with selected stratigraphic sections from Höskuldsson and Robin (1993), Siebe et al. (1993), Carrasco-Núñez and Rose (1995), and Rossotti and Nuñez (2004). Sections were described northeast of Sierra Negra and along the Encino River south of Pico de Orizaba. The inset maps show the location of the stratigraphic sections. Deposit thickness is to scale. (2-column fitting image). (For interpretation of the references to color in this figure legend, the reader is referred to the web version of this article.)

large carbonized tree logs are scattered at the base of the deposit, and vertical degassing pipes are locally observed, predominantly above the carbonized logs. Two of these carbonized logs yielded radiocarbon ages of  $8805 \pm 100$  yr BP (Table 1; section OR-6; Fig. 4c) and  $8890 \pm 90$  yr BP (Table 1; section OR-55; Fig. 5e) for Xil-1. A lens of rounded pumice fragments is observed above the ash-and-scoria pyroclastic flow in sections OR-56 and OR-83 (Fig. 4b). Charcoal collected from the pumice lens yielded a radiocarbon age of  $8785 \pm 90$  yr BP (Table 1; section OR-56; Fig. 5a).

## 5.2. Layer Xil-2 pf

This deposit lies above Xil-1 and is marked by a strong erosive contact. A thin layer of horizontally oriented burned grass and tree twigs is locally observed between Xil-1 and Xil-2 in section OR-61. Xil-2 consists of a massive and poorly sorted white-gray-pink pumice-and-ash flow deposit ranging from 0.8 to 5.3 m in thickness in sections OR-61 and OR-83 (Figs. 4b,c,d,f). The pumice fragments in Xil-2 are rounded and exhibit black-beige-white banding, with occasional gray angular xenoliths embedded within the juvenile fragments (sample OR-61A). A lens of rounded pumice fragments is observed above the pumice-and-scoria pyroclastic flow in section OR-61 (Fig. 4f).

## 5.3. Xil-3 pf

The base of Xil-3 is a ~2 cm-thick gray layer that contains abundant horizontally oriented burned grass and tree twigs. It rests in erosive contact on the pumice lens that overlies Xil-2 and is locally overlain by a thin, beige, consolidated, and massive to laminated fine-ash deposit (section OR-61; Figs. 4d,f).

These deposits are locally eroded and overlain by a 4.3-m-thick massive, poorly sorted, gray scoria-and-ash pyroclastic flow deposit (sections OR-6 and OR-61; Figs. 4a,d,f). This deposit is composed of black scoria fragments containing abundant small gray inclusions and small to large gray angular xenolith fragments embedded within the scoria fragments (sample OR-6E). A charcoal fragment collected at the base of Xil-3 yielded a radiocarbon age of  $8750 \pm 30$  yr BP (Table 1; section OR-61; Fig. 4d).

## 5.4. Xil-4 pf

This layer consists of a 3.9 to 5.8 m-thick massive, poorly sorted, gray block-and-ash flow deposit with numerous degassing pipes (sections OR-49, OR-61, OR-112, and OR-113; Figs. 4a, 5b,c,f, and 6c). This unit is distinguished at outcrop scale by its high abundance of block-sized gray lithic fragments (Figs. 5b,c,f, and 6c). Xil-4 is composed of black scoria that contains abundant small, rounded beige pumice nodules with some

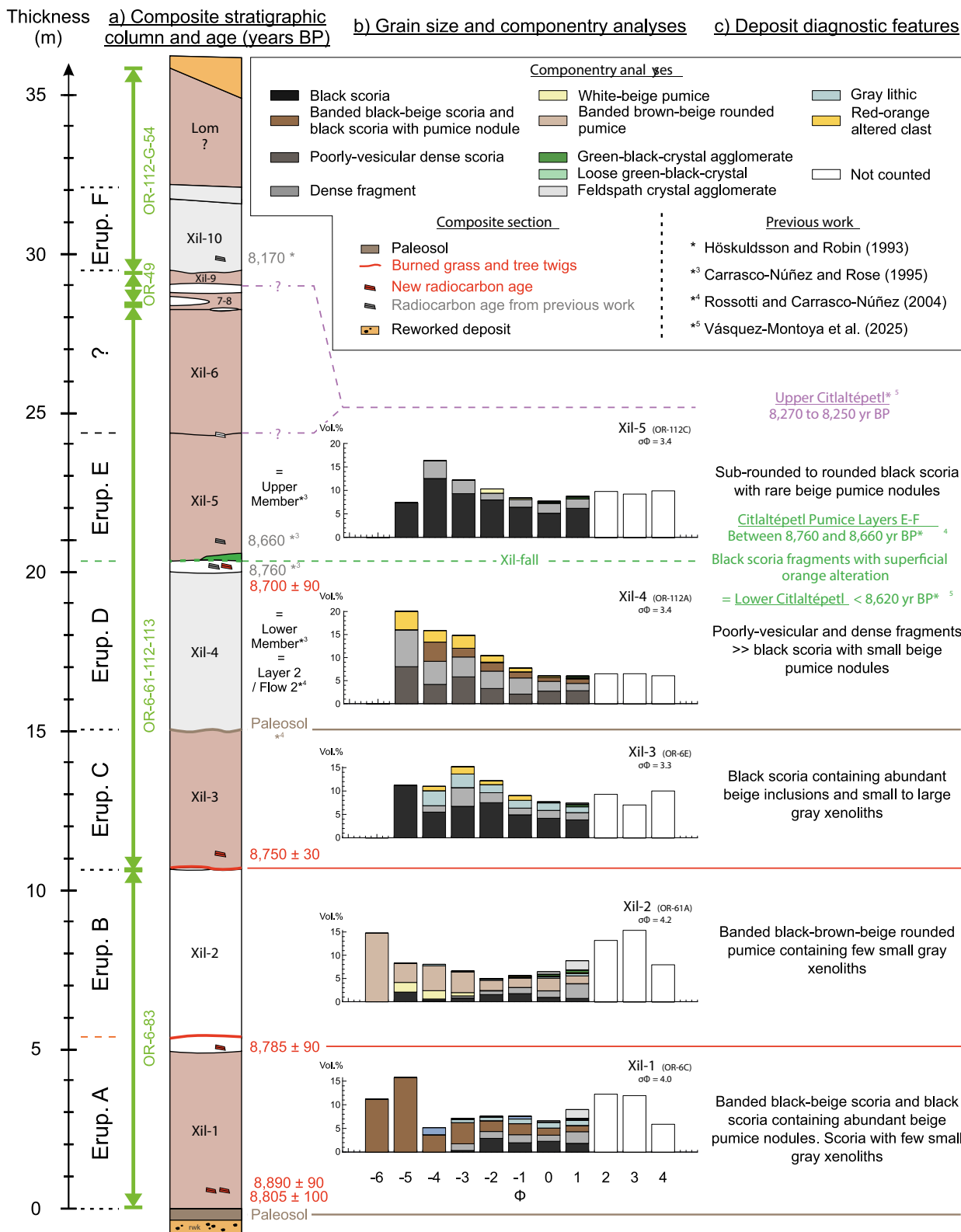


**Fig. 3.** a) Compound stratigraphic column showing the pyroclastic succession associated with the Xilomich, Loma Grande, Avalos, and Texmola eruptive episodes south of Pico de Orizaba. b) Grain size distribution and variation of the components through the stratigraphic succession. The orange, purple, green, and pink dashed lines indicate the inferred position of the Layer A, C, E-F, and H Citlaltépetl Pumice fallouts within the stratigraphic sequence. c) Resumed descriptions of the pyroclastic deposits south of Pico de Orizaba. Dates in gray are taken from Höskuldsson and Robin (1993) (\*), Carrasco-Núñez and Rose (1995) (\*<sup>3</sup>), and Rossotti and Núñez (2004) (\*<sup>4</sup>). Unit thickness is to scale. (2-column fitting image). (For interpretation of the references to color in this figure legend, the reader is referred to the web version of this article.)



**Fig. 4.** Field photographs of stratigraphic sections OR-6, OR-61, and OR-83 showing the Xil-1 to Xil-6 scoria-and-ash pyroclastic flows from the Xilomich eruptive episode exposed along the Encino River, west of Loma Grande. Radiocarbon dating of charcoal fragments from the pumice lenses above the Xil-1 and Xil-3 scoria-and-ash pyroclastic flows yielded radiocarbon ages of  $8805 \pm 100$  yr BP and  $8750 \pm 30$  yr BP, respectively. (2-column fitting image). (For interpretation of the references to color in this figure legend, the reader is referred to the web version of this article.)

gray angular xenoliths (samples OR-49A and OR-112A). A lens of rounded pumice fragments is observed above the pyroclastic flow deposit in section OR-49 (Fig. 6c). A charcoal fragment collected in this lens yielded a radiocarbon age of  $8700 \pm 90$  yr BP (Table 1; section OR-49; Fig. 6c).

### 5.5. Xil-fall

The Xil-4 pyroclastic flow deposit is overlain by a 5 cm-thick, clast-supported, well-sorted, medium- to fine-grained scoria pyroclastic fall deposit (Xil-fall) that is laterally continuous at outcrop scale but has been almost completely eroded by the overlying pyroclastic flow deposit (section OR-112; Fig. 5f). It has been entirely eroded in sections OR-61 and OR-113 (Figs. 4a and 5f). This deposit is made of black scoria

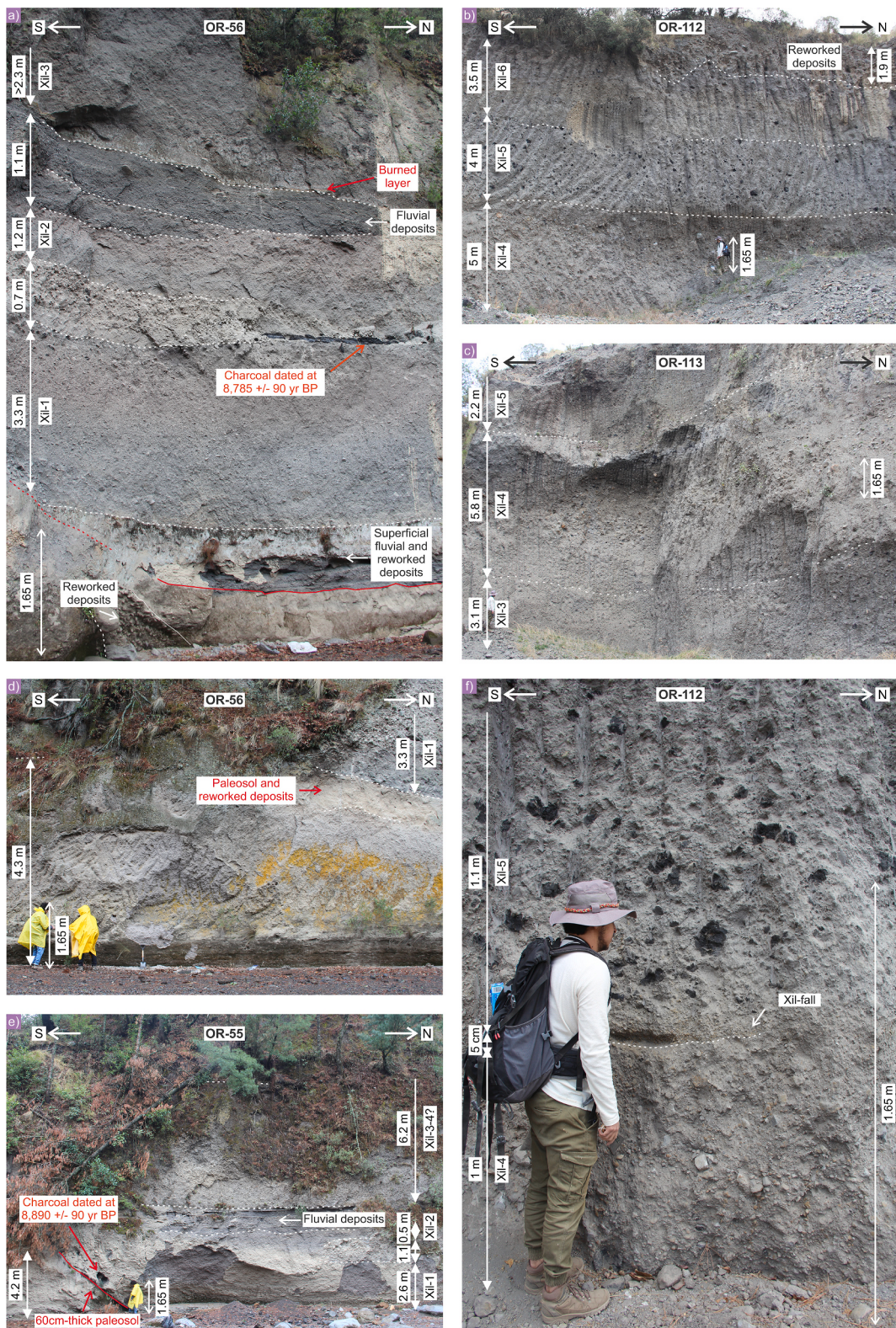


**Fig. 5.** Field photographs of the stratigraphic sections OR-55, OR-56, OR-112, and OR-113 showing the Xil-1 to Xil-6 scoria-and-ash pyroclastic flows exposed along the Encino River, west of Loma Grande and Texmola. Charcoal fragments from the base and overlying pumice lens of the Xil-1 pyroclastic flow yielded radiocarbon ages of  $8890 \pm 90$  yr BP and  $8785 \pm 90$  yr BP, respectively. Note the presence of the Xil-fall scoria pyroclastic fall layer between the Xil-4 and Xil-5 deposits. Observe the enrichment in lithic fragments in Xil-4 and the predominance of sub-rounded to rounded black scoria in the Xil-5 deposit. (2-column fitting image). (For interpretation of the references to color in this figure legend, the reader is referred to the web version of this article.)

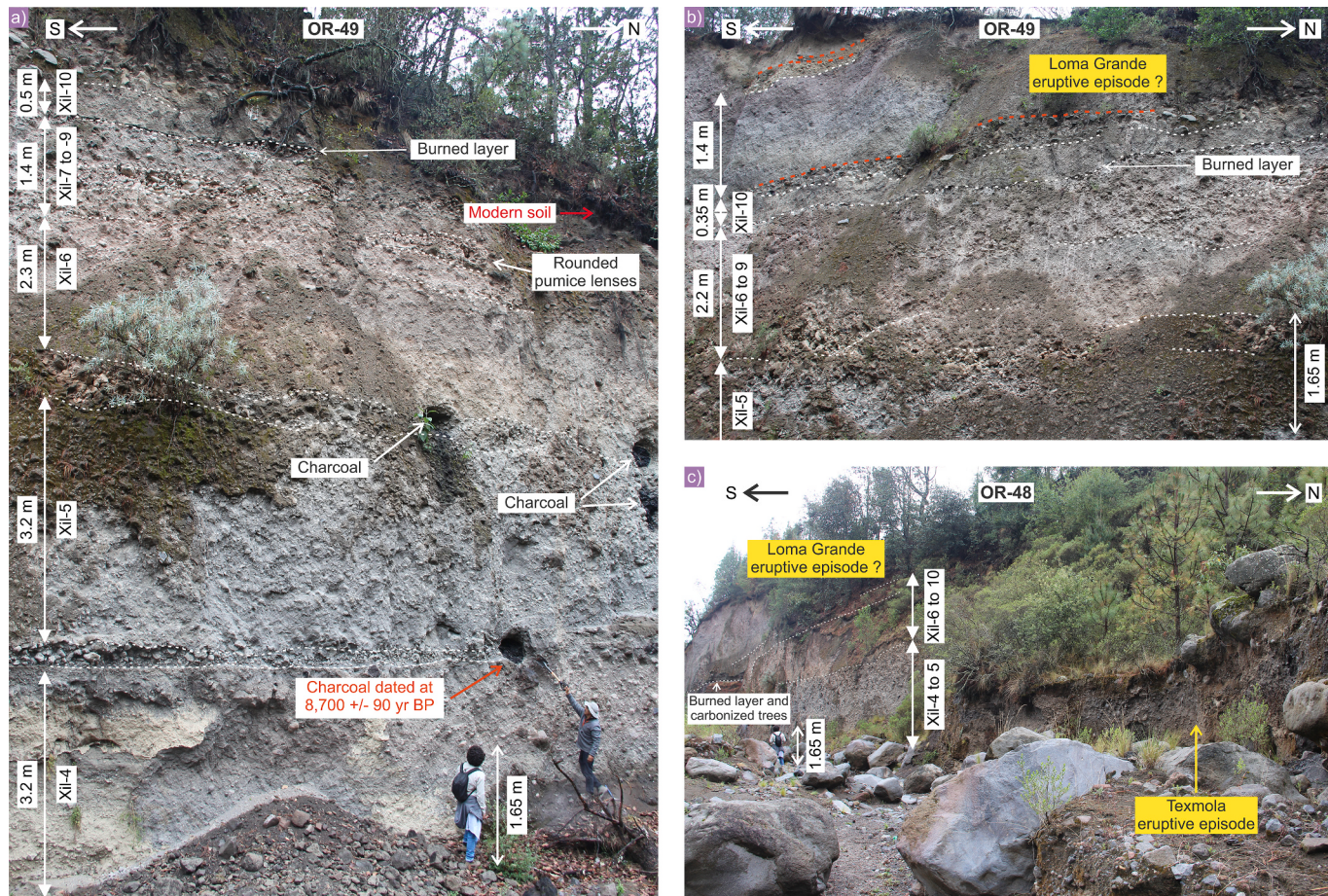


**Fig. 6.** Field photographs of stratigraphic sections OR-48 and OR-49 illustrating the Xil-4 to Xil-10 scoria-and-ash and block-and-ash pyroclastic flows of the Xilomich eruptive episode exposed along the Encino River, west of Texmola. Charcoal fragments from the pumice lens overlying Xil-4 yielded a radiocarbon age of  $8700 \pm 90$  yr BP. Note that the deposits of the Texmola eruptive episode are emplaced within erosional channels incised into the deposits of the Xilomich and possibly Loma Grande eruptive episodes. (2-column fitting image). (For interpretation of the references to color in this figure legend, the reader is referred to the web version of this article.)

fragments exhibiting orange surface alteration (sample OR-112B). The stratigraphic position of this fall layer, overlying deposits dated at 8700 yr BP, along with the characteristics of the scoria fragments, suggests that it may correspond to Layers E–F of the Citlaltépetl Pumice, dated between 8690 and 8660 yr BP (Rossotti and Nuñez, 2004), as well as with the Lower Citlaltépetl fallout found above a paleosol dated at 8620 yr BP (Vásquez-Montoya et al., 2025).

#### 5.6. Xil-5 pf

This deposit consists of a 2.5 to 4 m-thick massive and poorly-sorted scoria-and-ash flow. This layer is easily recognized by its abundance of subrounded to rounded scoria clasts that are white externally but black internally, with small beige pumice nodules enclosed within the fragments (Fig. 5b,c,d, and 6c), as well as the distinctly higher apparent vesicularity of the scoria fragments (sample OR-112C). This deposit corresponds to the pumice-and-ash flow deposit identified as the Upper Member / Flow 3 covering a thin pyroclastic fallout layer (Carrasco-Núñez and Rose, 1995; Rossotti and Nuñez, 2004). Carbonized wood fragments from the base of the pumice flow deposit yielded a radiocarbon age of 8660 yr BP in section #101 (Carrasco-Núñez and Rose, 1995). Carbonized wood fragments are observed at the contact between the Xil-5 pumice lens and the overlying deposit (Fig. 6a), although it was inaccessible for sampling for radiocarbon dating.

#### 5.7. Xil-6 to Xil-9 pf

Xil-5 is locally eroded by Xil-6, a 3.5 m-thick, apparently poorly sorted scoria-and-ash pyroclastic flow deposit with small black scoria fragments (sections OR-61 and OR-112; Fig. 4a and 5b). Xil-7 to Xil-9 is a metric-thick sequence of pyroclastic flow units delimited by well-defined pumice lens horizons (section OR-49; Figs. 6a,c). The Xil-6 to Xil-9 deposits could not be described due to limited accessibility. A black carbonized layer marks the top of the Xil-9 pyroclastic flow (Fig. 6a,c).

#### 5.8. Xil-10 pf

This layer could not be described directly due to limited access (section OR-49; Figs. 6a,c). However, the high concentration of dense rock fragments within the overlying lens horizon, the presence of large carbonized-wood fragments at the base, and its stratigraphic position collectively suggest a correlation with the block-and-ash flow deposit dated at  $8170 \pm 70$  yr BP in section G54 by Höskuldsson and Robin (1993).

### 6. Grain size and componentry analyses

#### 6.1. Grain size

The median grain size ( $\Phi_{50}$ ) of the Xil-1, Xil-3, and Xil-5 scoria-and-ash pyroclastic flow deposits ranges from  $-0.9$  to  $-1.9\Phi$ , with poor

sorting reflected in coefficients between 3.3 and 4.0 (Fig. 3) (Supplementary Material Table 2). These deposits also exhibit polymodal grain-size distributions (GSDs), with primary modes at  $-5\Phi$  for Xil-1,  $-3\Phi$  for Xil-3, and  $-4\Phi$  for Xil-5, along with a secondary population between 2 and  $3\Phi$  (Fig. 3). The Xil-4 block-and-ash flow has a  $\Phi_{50}$  ranging from  $-3$  to  $-3.2$  and exhibits similarly poor sorting, with coefficients between 3.4 and 3.9. It also displays an unimodal extended GSD with a mode at  $-5\Phi$ . The Xil-2 pumice-and-ash flow deposit has a  $\Phi_{50}$  of  $-0.7$  and is very poorly sorted. Its polymodal GSD, with a primary mode at  $-6\Phi$ , reflects the presence of block-sized fragments in the sample. The Xil-fall scoria pyroclastic fall deposit shows a  $\Phi_{50}$  of  $-2.5\Phi$  and a good sorting, with a coefficient of 1.8  $\Phi$ . In contrast to the other deposits, it presents a unimodal GSD with a mode between  $-2$  and  $-3\Phi$ . Variations in the components discussed below refer to the  $1\Phi$  grain-size fraction.

## 6.2. Componentry

Samples of the Xil-1 to Xil-5 pyroclastic deposits consist, in order of abundance of juvenile fragments (scoria, banded scoria, scoria with pumice nodules, banded pumice, pumice), black to dark-gray dense, gray lithic fragments, red-orange altered fragments, and crystal agglomerates (opx-cpx-ol and feldspar). Scoria fragments are often cauliflower-shaped with brown external chilled margins. These components vary in proportions with the location. The relative abundances of the components were assessed across the  $-6$  to  $1\Phi$  size sieve fractions (Fig. 3). Variations discussed in the text are referenced to the  $1\Phi$  fraction (Supplementary Material Tables 3, 4, and 5).

Diagnostic features, such as internal banding and pumice nodules within the scoria, the abundance of gray angular enclaves and feldspar agglomerates, and the overall textural properties of the juvenile fragments (Fig. 7), facilitated the correlation of the deposits across different stratigraphic sections. Combined with stratigraphic relationships and constrained by radiocarbon ages, these diagnostic criteria provide a robust framework for reconstructing the sequence and temporal evolution of the Xilomich eruptive episode.

The Xil-1 scoria-and-ash pyroclastic flow deposit (sample OR-6C) is notable for the presence of black-beige banded scoria and black scoria containing beige nodules and pumice lenses (14.1 vol%) and black scoria (22.9 vol%) (Figs. 3 and 7a-c). 27.4 vol% of subangular black to dark-gray dense fragments with rare vesicles were also recognized, while only 0.3 vol% of beige pumice clasts were counted in the  $1\Phi$  fraction. Gray angular enclaves ( $0.4 \times 0.4$  cm to  $2.3 \times 1.5$  cm), green-black glomerocrysts, and feldspar crystal agglomerates were also observed within the scoria fragments (Figs. 7a-c). Most of the light-colored inclusions observed within the scoria fragments correspond to crystal agglomerates. 2.5 vol% of green-black glomerocrysts (Opx-Cpx-Ol-Feld) and 20.5 vol% of feldspar agglomerates were counted as loose particles. Gray angular lithic fragments represent 12.2 vol% of the  $1\Phi$  fraction.

The Xil-2 pumice-and-ash pyroclastic flow deposit is characterized by sub-rounded to rounded black-brown-beige banded pumice clasts (18.8 vol%) and black scoria (8.2 vol%) (Figs. 3 and 7d-f). 35.3 vol% of

subangular black to dark-gray dense fragments with rare vesicles and less than 5.3 vol% of gray angular rock fragments were identified. 6.6 vol% of green-black glomerocrysts (Opx-Cpx-Ol-Feld) and 22.2 vol% of feldspar agglomerates were counted in the  $1\Phi$  fraction (sample OR-6A).

The Xil-3 scoria-and-ash flow deposit contains black scoria with abundant gray inclusions and numerous gray angular enclaves, up to  $2.5 \times 3.3$  cm, embedded within the scoria fragments (51.6 vol%) (Figs. 3 and 7g-i). Most of the gray inclusions correspond to feldspar and green-black crystal agglomerates. This sample also contains black to dark-gray dense fragments with rare vesicles (20.9 vol%). A notable enrichment in gray angular rock fragments was observed in the sample (16.8 vol%). These fragments are similar to those found as enclaves within the scoria. 7.0 vol% of green-black glomerocrysts (Opx-Cpx-Ol-Feld) and only 3.0 vol% of feldspar agglomerates were counted in the  $1\Phi$  fraction (sample OR-6E).

The Xil-4 block-and-ash flow deposit is distinguished by a high abundance of black scoria-shaped fragments (46.6 vol%) (Fig. 3); however, these fragments are denser with fewer vesicles than the scoria described in the previous samples. This sample contains abundant black to dark-gray subangular dense fragments with rare vesicles, and bread-crust external fractures (26.3 vol%) (Fig. 7l). These fragments are denser than scoria but lighter than typical rock fragments. Additionally, 17.0 vol% of cauliflower-shaped black scoria fragments containing beige pumice nodules were identified (Figs. 7j-k). These fragments are similar to the scoria fragments observed in the other samples. 4.1 vol% of green-black glomerocrysts (Opx-Cpx-Ol-Feld) and only 1.5 vol% of feldspar agglomerates were counted in the  $1\Phi$  fraction of the deposits (sample OR-112A).

The Xil-fall scoria pyroclastic fall deposit is composed of sub-angular to sub-rounded brown to black scoria fragments, often exhibiting orange surface alteration (70.0 vol%) and subangular black to dark-gray dense fragments (23.4 vol%). 4.5 vol% of green-black glomerocrysts (Opx-Cpx-Ol-Feld) and 2.8 vol% of feldspar agglomerates were counted in the  $1\Phi$  fraction (sample OR-112B).

The Xil-5 scoria-and-ash pyroclastic flow deposit stands out for its high concentration of cauliflower-shaped to rounded black scoria fragments (70.3 vol%) (Figs. 3 and 7m-o). A few beige pumice inclusions were observed within the scoria fragments on the outcrop scale. 23.1 vol% of subangular black to dark-gray dense fragments were also identified. A total of 5.2 vol% of green-black glomerocrysts (Opx-Cpx-Ol-Feld) and 1.4 vol% of feldspar agglomerates were counted in the  $1\Phi$  fraction (sample OR-112C).

## 7. Petrography

Six thin sections of scoria, pumice, and block fragments from the Xil-1 to Xil-5 pyroclastic flow deposits were examined under the petrographic microscope to characterize their mineral assemblages and textural features (Fig. 8). The modal analysis (in percent) referenced in the text is provided in Table 2. The number of counts (#) and crystal size are specified in Supplementary Material Table 6.

**Table 2**

Modal analysis of scoria, pumice, and poorly vesicular fragments of the Xil-1 to Xil-5 pyroclastic units. Microphenocrysts (0.03 to 0.3 mm) and phenocrysts ( $> 0.3$  mm) were measured.

Unit	Thin section	Material	Plg	Cpx	Opx	Amp	Ol	Fe-Ti ox	Gmass*	Ves	Rock	Total (%)
Xil-1	OR-6C	Scoria	6	2.5	1	5.8	0	0	74.5	10.2	0	100
Xil-2	OR-61A	Pumice	10.3	3	0.4	1.6	0	0	47.2	36.9	0.6	100
Xil-3	OR-6E	Scoria	10.6	4.3	2.4	0	1.4	0	58.8	22.5	0	100
Xil-3	OR-6E	Enclave	72.2	7.8	0.5	0	16.3	3.2	0	0	0	100
Xil-4	OR-112A	Scoria	8.3	5.5	1.6	0	0	0	49.8	34.8	0	100
Xil-4	OR-112A	Dense	23.2	1.5	0.4	4.5	0	0.4	61.6	8.4	0	100
Xil-5	OR-112C	Scoria	8.9	6.8	2.2	0	0	0	47.8	34	0.3	100

Plg = plagioclase, Cpx = clinopyroxene, Opx = orthopyroxene, Amp = amphibole, Ol = olivine, Fe-Ti ox = Fe-Ti oxides, Gmass\* = groundmass = microlites + glass, and Ves = vesicles. (1-column fitting table).

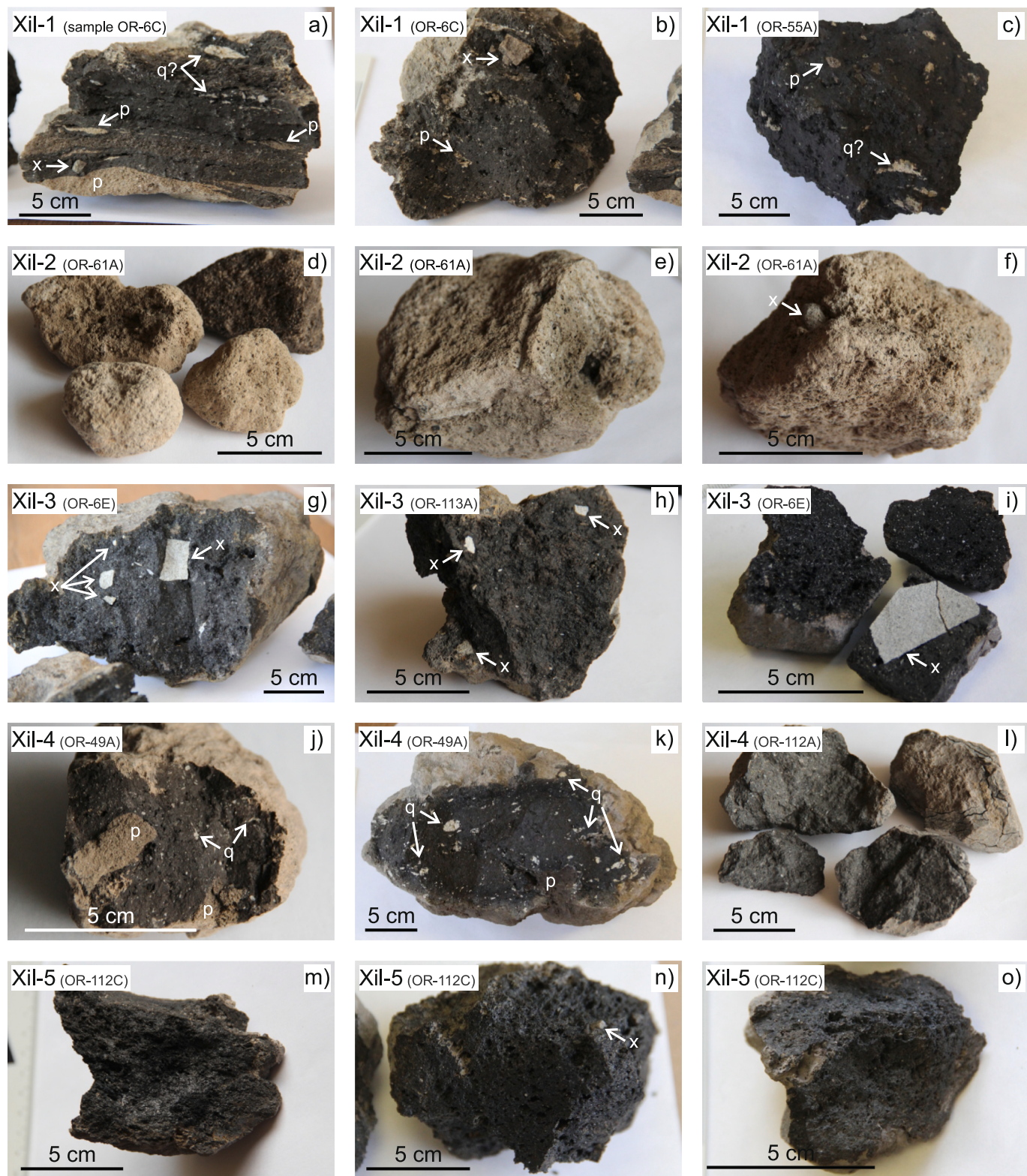


**Fig. 7.** Photographs of scoria, pumice, and poorly vesicular dense fragments of the Xil-1 to Xil-5 pyroclastic flow deposits, collected in the Encino River south of Pico de Orizaba. Abbreviations are: p = pumice, q = quartzite, and x = xenolith. (a-c) Banded black-beige scoria and black scoria containing abundant beige pumice nodules of the Xil-1 pyroclastic flow. Note the presence of a small gray angular xenolith and quartzite lenses in picture (a). (d-f) Banded black-brown-beige rounded pumice fragments containing few small gray xenoliths of Xil-2. Note the color change in the pumice fragments in picture (a) and the color variations in the fragment in pictures (b) and (c). (g-i) Black scoria containing abundant beige inclusions and small to large gray angular xenoliths of Xil-3. (j-l) Black scoria with beige pumice nodules in pictures (j) and (k), and poorly vesicular dense fragments in picture (l) of the Xil-4 pyroclastic flow. Note the presence of quartzite in the scoria fragments. (m-o) Sub-rounded to rounded black scoria. Note the higher vesicularity of the scoria fragment. (2-column fitting image). (For interpretation of the references to color in this figure legend, the reader is referred to the web version of this article.)

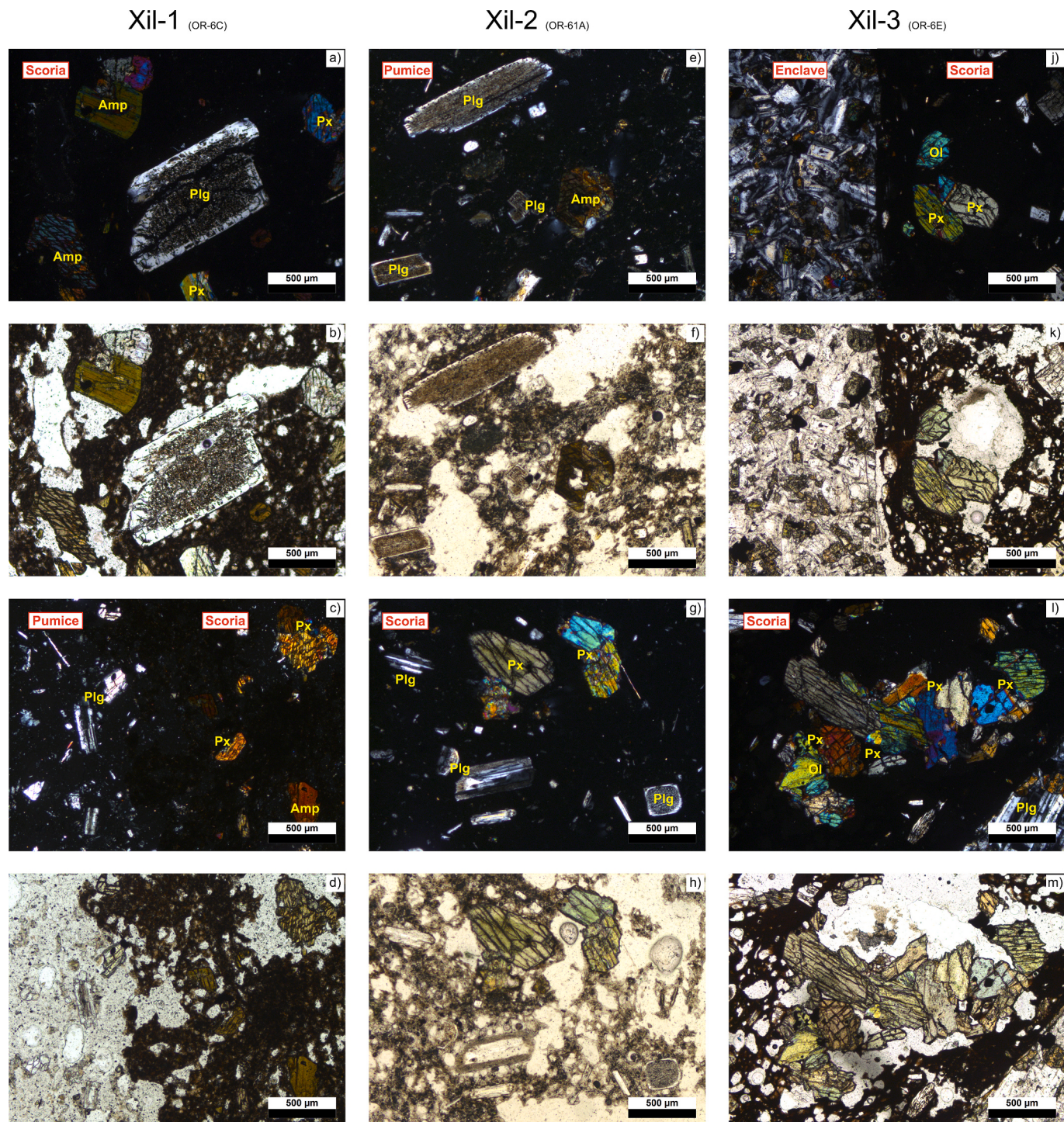


**Fig. 8.** Microphotographs of scoria, pumice, and poorly vesicular fragments of the Pico de Orizaba Xil-1 to Xil-5 pyroclastic flows. Plg = plagioclase; Opx = orthopyroxene; Cpx = clinopyroxene; Ol = olivine; Amp = amphibole. Note the sieve texture in both individual plagioclase and plagioclase agglomerates in the pictures Xil-1, Xil-2, Xil-4, and Xil-5. Observe the pyroxene glomerocrysts in the scoria and pumice fragments in pictures Xil-1, Xil-2, Xil-3, Xil-4, and Xil-5. (2-column fitting image). (For interpretation of the references to color in this figure legend, the reader is referred to the web version of this article.)

All the scoria and pumice fragments display porphyritic, hypocrystalline, glomeroporphyritic, and vesicular textures (Fig. 8). They show significant textural variations, including banded black-beige scoria (Xil-1; Figs. 8c-d), black scoria with beige pumice nodules (Xil-1 and Xil-4; Figs. 8a-b and n-q), rounded banded black-brown-beige pumice (Xil-2; Figs. 8e-h), and vesicular black scoria (Xil-3 and Xil-5; Figs. 8j-m and v-y). Scoria fragments from Xil-3 contain abundant gray angular

enclaves (Figs. 8j-k). The poorly vesicular clast of Xil-4 exhibits a porphyritic, hypocrystalline, and glomeroporphyritic texture (Figs. 8r-u). The total crystal content of scoria and pumice ranges from 15.3 to 18.7 vol%, while 30 vol% and 100 vol% crystal contents were observed in the Xil-4 poorly vesicular and Xil-3 enclave fragments, respectively (Table 2). After plagioclase (6 to 10.6 vol%), clinopyroxene and, to a lesser extent, orthopyroxene are the most abundant crystalline phases in

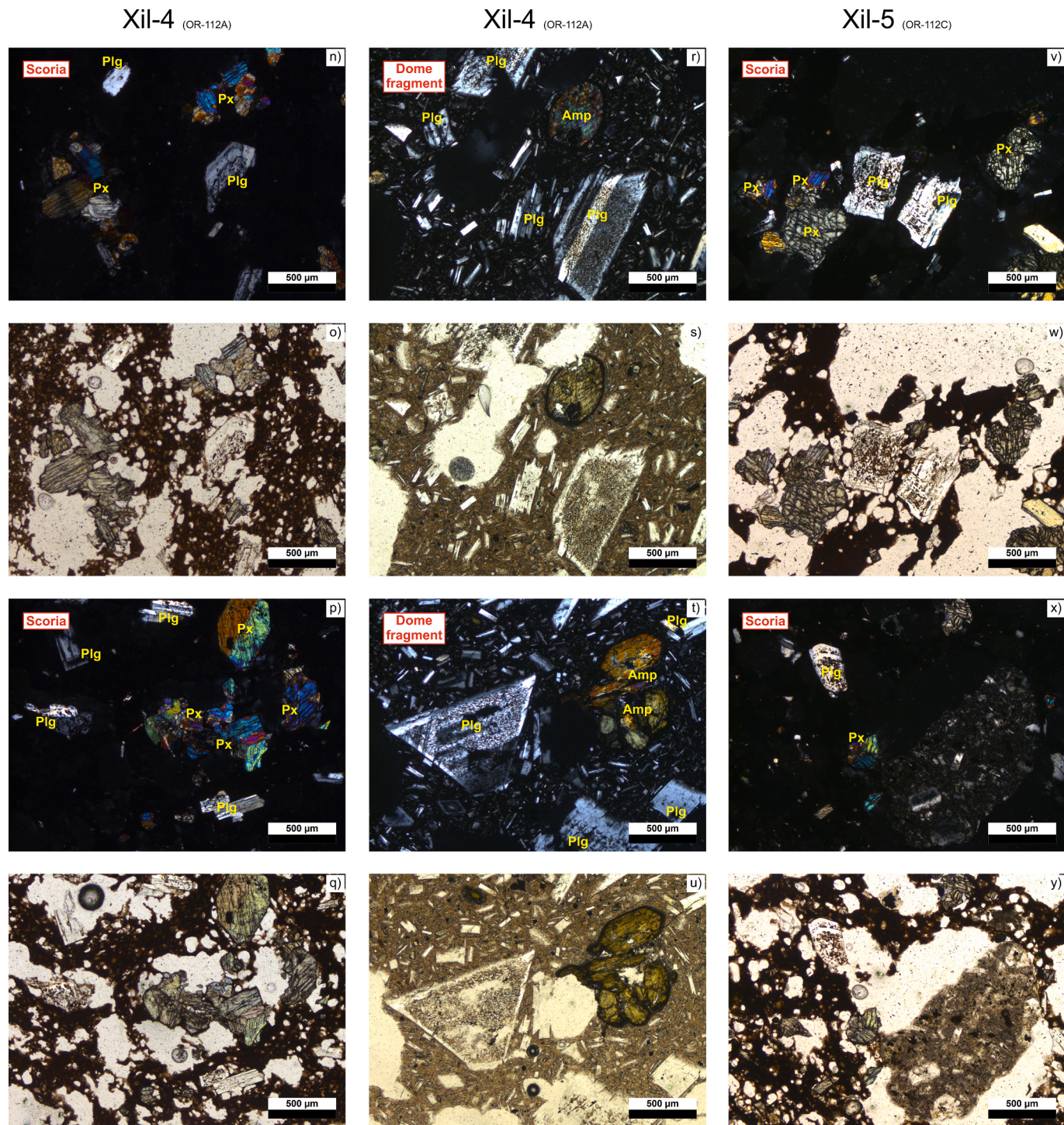


Fig. 8. (continued).

the scoria and pumice fragments, with abundances ranging from 3.5 to 9.0 vol% (Figs. 8). Amphibole was only found in the Xil-1 and Xil-2 scoria and pumice (1.6 to 5.8 vol%) (Figs. 8a-d and e-h), and in the Xil-4 poorly vesicular fragment (4.5 vol%) (Figs. 8r-u). Olivine is present exclusively in the Xil-3 scoria (1.4 vol%) and Xil-3 enclave (16.3 vol%) fragments (Figs. 8j-m). Groundmass represents 47.2 to 58.8 vol% in the Xil-2 to Xil-5 scoria and pumice fragments (Figs. 8e-h, j-m, n-q, and v-y), whereas the Xil-1 scoria exhibits a higher groundmass proportion of 74.5 vol% (Figs. 8a-d). This pattern is reflected in the vesicle content, which ranges from 22.5 to 36.9 vol% in the Xil-2 to Xil-5 pumice and scoria fragments, while the Xil-1 scoria contains significantly fewer

vesicles, with only 10.2 vol%.

Scoria fragments from the Xil-3 and Xil-5 units contain two types of light-colored fragments: diorite enclaves and quartzite xenoliths. The diorite enclaves display a holocrystalline and inequigranular texture and are composed mostly of subhedral plagioclase (72.2 vol%), olivine (16.3 vol%), clinopyroxene (7.8 vol%), orthopyroxene (0.5 vol%), and Fe-Ti oxide (3.2 vol%) crystals (Figs. 8j-k). They are made of the same mineral assemblage as the host scoria but are notably more enriched in olivine. In contrast, the quartzite xenoliths are composed of polycrystalline quartz and glass. Quartz crystals within these fragments are anhedral and display undulatory extinction, whereas the accompanying glass

presents a light brown coloration.

## 8. Discussion

### 8.1. Reinterpretation of the Xilomich eruptive episode

Reported dates of the Xilomich eruptive episode (8710 to 8170 yr BP; sections G54 and R60; Höskuldsson and Robin, 1993) and the Citlaltépetl Ignimbrite and Pumice sequences (8980 to 8455 yr BP; sections PO-78 and HV14320; Carrasco-Núñez and Rose, 1995; Rossotti and Nuñez, 2004) indicate that these events occurred during the same period. By incorporating the radiocarbon date of 8980 yr BP reported by Carrasco-Núñez and Rose (1995), the duration of the Xilomich eruptive episode, initially defined as occurring between 8710 and 8170 yr BP by Höskuldsson and Robin (1993), is extended from 8980 to 8170 yr BP. This revised time frame indicates a longer and more complex period of volcanic activity for the Xilomich eruptive episode, lasting approximately 810 years (Fig. 9).

Previous stratigraphic sections and age determinations (8–9 ka) for the Citlaltépetl Ignimbrite and Xilomich eruptive episode (Supplementary Material Table 7) provide limited stratigraphic and chronological constraints in the southern sector of Pico de Orizaba (Fig. 9).

In this work, we describe the pyroclastic sequence deposited between 8000 and 9000 yr BP south of Pico de Orizaba. This reinterpretation is based on new field observations, petrographic descriptions, granulometric and componentry analyses, and new age constraints. Five additional radiocarbon dates ranging from  $8890 \pm 90$  to  $8700 \pm 90$  yr BP were obtained to refine the timing of pyroclastic activity in the southern sector of the volcano (Table 1; Supplementary Material Table 7).

Because the pyroclastic flow deposits in the study area are numerous, visually similar, and closely spaced in age, age determinations alone are insufficient to differentiate units. Description of the juvenile fragments, scoria-pumice textures (black, banded black-brown-beige, black with white inclusions), gray angular rock fragments, and the abundance of feldspar and crystal agglomerates (Figs. 7 and 8) allowed us to establish a diagnostic fingerprint for the juvenile clasts of the pyroclastic flow identified south of Pico de Orizaba. Combining field observations and radiocarbon dates with this fingerprint helped us to correlate the pyroclastic flows observed in the study area and to provide a detailed characterization of the deposits.

We also integrate selected stratigraphic descriptions from previous studies (Höskuldsson and Robin, 1993; Siebe et al., 1993; Carrasco-Núñez and Rose, 1995; Rossotti and Nuñez, 2004; Rossotti et al., 2006) (Fig. 2). Although Höskuldsson and Robin (1993) did not provide coordinates for their stratigraphic sections, approximate UTM coordinates were determined by georeferencing their Fig. 6 map using ArcMap version 10.8. In addition to our new data (sections OR-#), we integrate and compare the findings of these earlier studies, which were previously uncorrelated, to develop a more comprehensive understanding of the pyroclastic succession (Figs. 3 and 9).

Our new set of radiocarbon ages dates three previously undescribed pyroclastic flow units south of Pico de Orizaba, Xil-1 ( $8890 \pm 90$  to  $8785 \pm 90$  yr BP), Xil-2 (between  $8785 \pm 90$  and  $8750 \pm 30$  yr BP), and Xil-3 ( $8750 \pm 30$  yr BP), and provide additional ages that better constrain the timing of Xil-4 ( $8700 \pm 90$  yr BP) (Fig. 2). These ages are consistent with the 8980–8660 yr BP ages reported for the Lower and Upper Members (Carrasco-Núñez and Rose, 1995) and Flow 1/Layer 1 to Flow 4/Layer 4 (Rossotti and Nuñez, 2004; Rossotti et al., 2006) pyroclastic deposits of

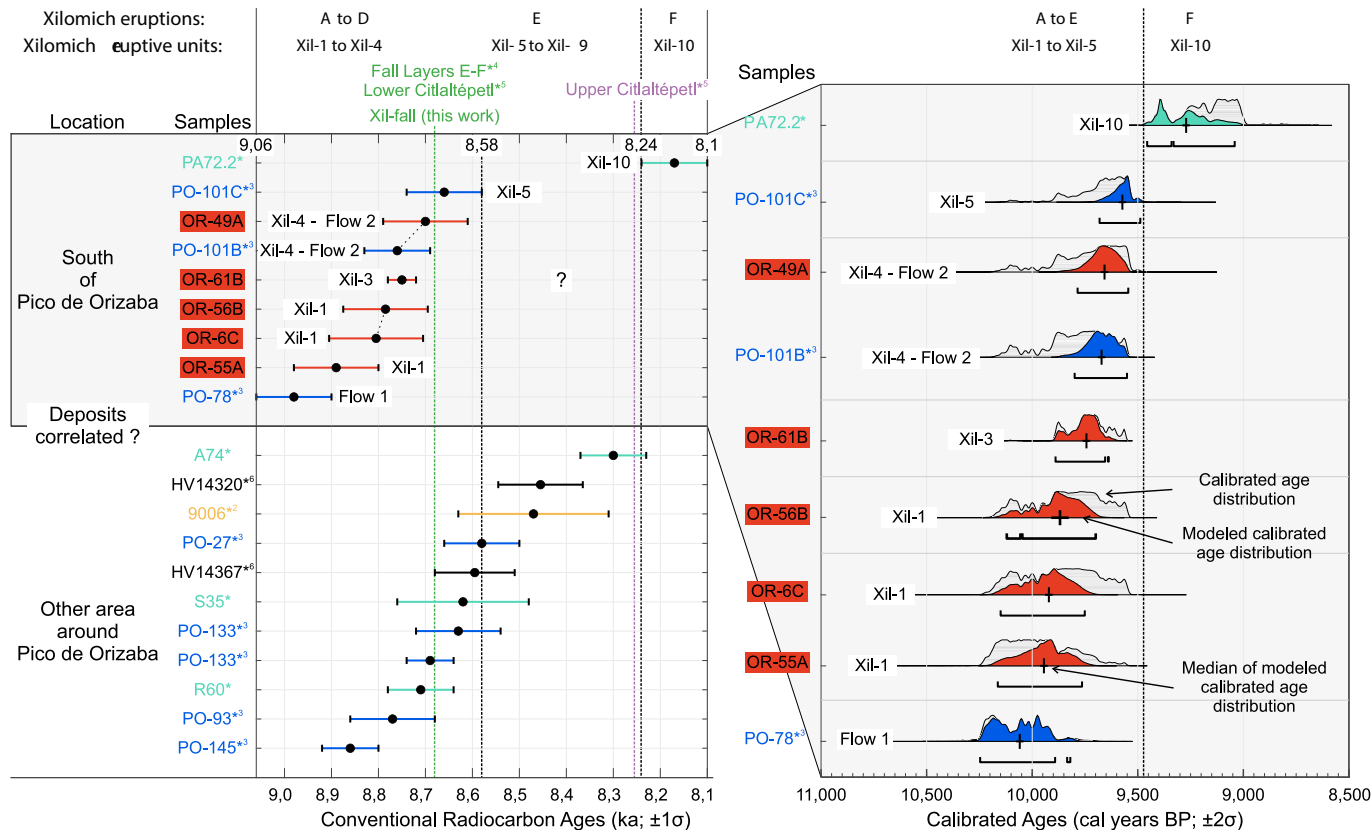


**Fig. 9.** Diagram showing conventional radiocarbon ages (left) and calibrated ages (right) for pyroclastic flow deposits emplaced during the Xilomich eruptive episode, including our samples (south of Pico de Orizaba) and previous works: Höskuldsson and Robin (1993) (\*), Siebe et al. (1993) (\*<sup>2</sup>), Carrasco-Núñez et al. (1993) and Carrasco-Núñez and Rose (1995) (\*<sup>3</sup>), and Heine (written communication, 1992) (\*<sup>6</sup>). The ages of the Lower Citlaltépetl (Fall Layers E-F) and the Upper Citlaltépetl from Rossotti and Nuñez (2004) (\*<sup>4</sup>) and Vásquez-Montoya et al. (2025) (\*<sup>5</sup>) are in purple and green. (2-column fitting image). (For interpretation of the references to color in this figure legend, the reader is referred to the web version of this article.)

the Citlaltépetl Ignimbrite (Fig. 9). The calibrated ages of the samples are statistically similar, 10228–9688 (9985) to 10121–9530 (9703) cal BP, indicating emplacement within a short period, consistent with the conventional radiocarbon ages (Fig. 9). The implementation of a Bayesian stratigraphic Sequence in OxCal v4.4.4, with radiocarbon samples grouped by pyroclastic unit and ordered according to field stratigraphy, yielded modeled calibrated ranges that are narrower than the unmodeled distributions (“with model” and “without model” in Supplementary Material Table 7), allowing clearer age differentiation across southern-sector deposits (Fig. 9).

Correlation of our OR-# stratigraphic sections with those of Carrasco-Núñez and Rose (1995; e.g., #78 and #101), Rossotti and Nuñez (2004); e.g., C-02-25), and Höskulsson and Robin (1993; e.g., G54 and R60), enabled the correlation of several of our Xil-# units to well-documented pyroclastic flow units of the Citlaltépetl Ignimbrite and Xilomich eruptive episode (Fig. 3). This correlation revealed that most deposits south of Pico de Orizaba, specifically Xil-1, Xil-2, Xil-3, Xil-6, and Xil-7 to Xil-9, had not been described in previous studies. Our new sequence contrasts with the four pyroclastic flow model (Flow 1/Layer 1 to Flow 4/Layer) proposed by Rossotti and Nuñez (2004) and Rossotti et al. (2006). This data indicate that at least three pyroclastic flow deposits were emplaced between Flow 1/Layer 1 and Flow 2/Layer 2 deposits, suggesting that the southern sector of Pico de Orizaba experienced more intense explosive activity during the Xilomich eruptive episode.

Within this framework, the 8980 yr BP scoria-pumice and ash flow deposit documented in the Maltrata area (section #78; Carrasco-Núñez and Rose, 1995) correlates with Flow 1/Layer 1 of Rossotti and Nuñez (2004) and Rossotti et al. (2006). The observed differences in age and uncertainty between PO-78 and OR-6C suggest that Flow 1/Layer 1 represents a pyroclastic flow older than Xil-1 and likely represents the earliest pyroclastic flow unit of the Xilomich eruptive episode emplaced south of Pico de Orizaba.

The Xil-1 scoria-and-ash pyroclastic flow was emplaced between  $8890 \pm 90$  and  $8785 \pm 90$  yr BP (sections OR-6, OR-55, and OR-56; Figs. 4c,e and 5a,e) above a 30–60 cm-thick paleosol interpreted to have developed through ~500–1000 years (E. Solleiro, pers. comm.) in the Encino River south of Pico de Orizaba. The componentry and stratigraphic position of the pyroclastic flow deposit dated to  $8890 \pm 90$  yr BP above the ~60 cm-thick paleosol (OR-55; Fig. 5e) are consistent with correlation to the Xil-1 deposit of section OR-6. However, an older, near-coeval deposit cannot be excluded (Fig. 9). Spatial proximity and similarity in deposit characteristics may suggest that the  $8805 \pm 100$  yr BP Xil-1 unit (section OR-6; this work) corresponds to the Flow 1/Layer 1 scoria-and-ash at nearby section C-02-25 (Rossotti and Nuñez, 2004; Rossotti et al., 2006).

Following Xil-1, between  $8785 \pm 90$  and  $8750 \pm 30$  yr BP (this work; Fig. 4), the Xil-2 pumice-and-ash flow was emplaced. Burned grass and tree twigs beneath Xil-2 indicate a brief pause between Xil-1 and Xil-2.

Shortly thereafter, at  $8750 \pm 30$  yr BP (this work; Fig. 4), the Xil-3 scoria-and-ash flow deposit was emplaced above burned grass and tree twig fragments. Its stratigraphic position supports correlation with the undescribed deposit reported between a lahar and a paleosol at Paso Carretas (section C-02-25; Rossotti and Nuñez, 2004).

Based on the spatial proximity of section OR-49 to #101 and the similarity of deposits and ages in both sections, we interpret the Xil-4 block-and-ash flow deposit as the deposit of the Lower Member and Flow 2/Layer 2 of the Citlaltépetl Ignimbrite (Carrasco-Núñez and Rose, 1995; Rossotti and Nuñez, 2004). Likewise, the pumice lens that overlies Xil-4, dated at  $8700 \pm 90$  yr BP (this work; Fig. 6a), corresponds to the pumice flow deposit dated at 8760 yr BP (section #101; Carrasco-Núñez and Rose, 1995). We interpret that the Xil-4 block-and-ash flow was deposited between 8760 and 8700 yr BP above the paleosol exposed at Paso Carretas (section C-02-25; Rossotti and Nuñez, 2004).

Shortly thereafter, the Xil-fall deposit was deposited above Xil-4 (section OR-112; Fig. 5f). This layer that can be correlated with the

Layers E-F pyroclastic fall deposits, which lies between the pyroclastic flow deposits of the Lower Member (Xil-4, Layer 2/Flow 2) dated between 8760 and 8700 yr BP (sections #101, C-02-25, and OR-49; Carrasco-Núñez and Rose, 1995; Rossotti and Nuñez, 2004; this work) and the Upper Member (Xil-5), dated at 8660 yr BP (section #101; Carrasco-Núñez and Rose, 1995). The age range of this fall layer (8700–8660 yr BP) also suggests a correlation with the Lower Citlaltépetl fallout dated at 8620 yr BP by Vásquez-Montoya et al. (2025).

During emplacement of the Xil-5 scoria-and-ash pyroclastic flow deposit, the underlying Xil-fall deposit was almost entirely eroded. Xil-5 correlates with the Upper Member of the Citlaltépetl Ignimbrite, dated at 8660 yr BP at section #101 (Carrasco-Núñez and Rose, 1995).

Above Xil-5, access was not possible, preventing the description of the overlying units. However, the presence of interbedded pumice lenses at section OR-49 (Fig. 6) may indicate deposition of at least four pyroclastic flow units (Xil-6 to Xil-9). Their stratigraphic position beneath the 8170 yr BP block-and-ash flow (Höskulsson and Robin, 1993) suggests correlation with the ash-tuff layers interlayered with the scoria lapilli beds of the Upper Citlaltépetl, dated between 8270 and 8250 yr BP (Vásquez-Montoya et al., 2025). Likewise, the presence of large carbonized tree trunks at the base of the pyroclastic flow deposit and the lens of block fragments overlying the deposit support its correlation with the block-and-ash flow dated at 8170 yr BP by Höskulsson and Robin (1993).

Most of the pyroclastic flow units described above are separated by lenses of subrounded to rounded pumice fragments (Figs. 4, 5, and 6). Similar to those documented in the 1993 pyroclastic flows of Lascar volcano, Chile (Calder et al., 2000), these lenses are interpreted as the product of buoyant segregation of pumice clasts, which were transported upward and laterally along the margins of high-concentration basal flow layers. Along with pumice lenses, pyroclastic flows are separated by either paleosols (between Xil-3 and Xil-4), layers containing horizontally oriented burned grass and tree twigs (between Xil-1 and Xil-2; Xil-2 and Xil-3), or pyroclastic fall deposits (Xil-fall in this work; Layers E-F of the Citlaltépetl Pumice). These features record episodes of quiescence between flow emplacement events, during which surface conditions stabilized sufficiently to permit vegetation growth and soil development. The absence of interbedded paleosol or burned grass and tree twig between Xil-5 and Xil-9 likely suggests they were produced by the same eruptive event. However, these deposits could also be separate pyroclastic flow units, which could be better recorded at other sites. These indicators of temporal breaks suggest that the ten identified pyroclastic flow deposits (Xil-1 to Xil-10) were emplaced during at least six distinct eruptions between 8980 and 8170 yr BP (labeled Erup. A to F in Fig. 3).

## 8.2. Eruption mechanism

The stratigraphic descriptions and componentry analyses of the pyroclastic flow deposits indicate that the Xilomich eruptive episode, which occurred between 8980 and 8170 yr BP, comprised at least four Vulcanian-type eruptions (Xil-1, Xil-3, Xil-5, Xil-6) and two dome-destruction events (Xil-4 and Xil-10).

Following the interpretation of Rossotti et al. (2006) regarding the formation of the scoria-rich pyroclastic flow deposits of the Citlaltépetl Ignimbrite (8980–8455 yr BP), we infer that the  $8890 \pm 90$  to  $8785 \pm 90$  yr BP Xil-1,  $8750 \pm 30$  yr BP Xil-3, 8660 yr BP Xil-5, and Xil-6 scoria-and-ash pyroclastic density currents were generated during fountain collapse of material ejected into the atmosphere during short-lived Vulcanian explosions, through detachment of the lower portions of the Vulcanian columns. The presence of poorly vesicular accidental lithics (20.9–35.3 vol%) in the Xil-1, Xil-3, and Xil-5 scoria-and-ash and pumice-and-ash pyroclastic flows may represent remnants of the conduit plugs that were fragmented during the overpressurization process prior to these eruptive events. The injected mafic magma, likely enriched in dissolved volatiles, may have generated overpressure beneath the

conduit plugs in the crater of Pico de Orizaba. The cauliflower shape and external chilled margins of the scoria fragments may also suggest interaction between the pyroclastic flows and ice from Pico de Orizaba glacier, as proposed by Macías et al. (2020) to explain the morphology of the scoria fragments from the 2001 Vulcanian eruption of Popocatépetl volcano.

The Xil-2 pumice-and-ash flow, dated between  $8785 \pm 90$  and  $8750 \pm 30$  yr BP (this work), may correspond to a pyroclastic flow generated by the collapse of an eruptive column, similar to that observed during the third phase of the 1913 eruption of Colima volcano (Saucedo et al., 2010).

In contrast, the Xil-4 and Xil-10 block-and-ash flow deposits are

attributed to dome destruction events that occurred at approximately 8760–8700 and 8170 yr BP, respectively (this work; Höskuldsson and Robin, 1993). The presence of scoria fragments within the Xil-4 deposit suggests that strong Vulcanian explosions triggered the partial or total destruction of a dome, similar to that proposed during the eruptive activity of Popocatépetl volcano (Gómez-Vazquez et al., 2016). Gas accumulation resulting from the exsolution of volatiles originally dissolved in the mafic magma may have generated overpressure beneath the dome formed during previous eruptions within the crater of Pico de Orizaba, ultimately leading to dome failure and Soufrière-type collapse. This interpretation is consistent with the high proportion of dense black scoria (46.6 vol%) and poorly vesicular fragments (26.3 vol%) observed

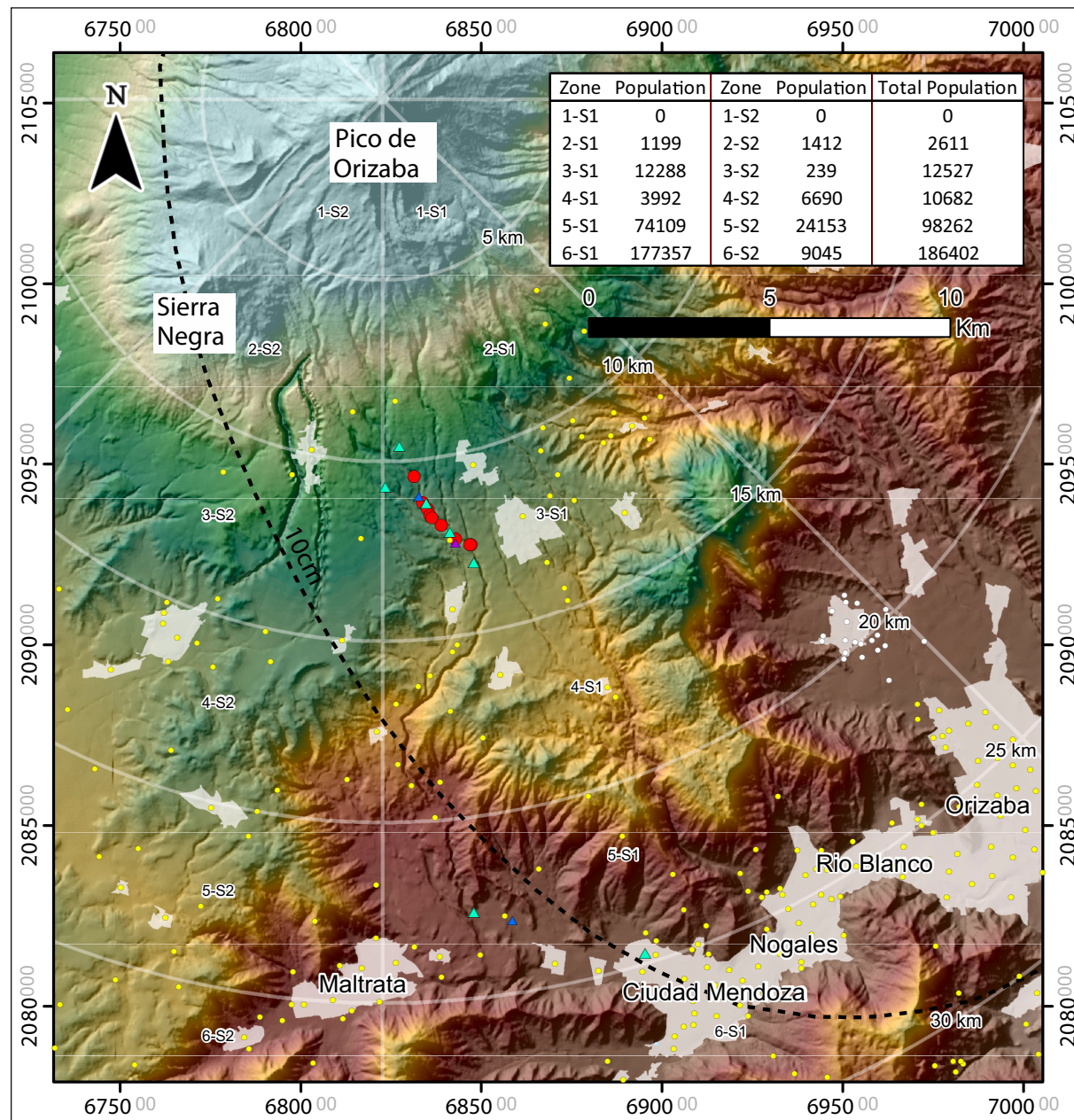


**Fig. 10.** Shaded relief model showing the distribution of population south of Pico de Orizaba. Yellow points correspond to rural localities and centroids of AGEB population areas based on the 2020 INEGI data (National Institute of Statistics and Geography (INEGI), 2020a; National Institute of Statistics and Geography (INEGI), 2020b; National Institute of Statistics and Geography (INEGI), 2020c). Red points mark the stratigraphic sections described in this study, while green, blue, and purple triangles represent the stratigraphic sections from Höskuldsson and Robin (1993), Carrasco-Núñez and Rose (1995), and Rossotti and Nuñez (2004). The black dashed lines delineate the 10 cm isopach contour of Citlaltépetl Pumice Layer F (Rossotti et al., 2006). Coordinates follow the UTM Zone 14 projection based on the WGS84 ellipsoid, displayed at a 1:100,000 scale. (2-column fitting image). (For interpretation of the references to color in this figure legend, the reader is referred to the web version of this article.)

in the Xil-4 block-and-ash pyroclastic flow.

The eruptive behavior of Pico de Orizaba, characterized by alternating phases of lava emission, dome growth and collapse, and short-lived Vulcanian-type explosions, resembles that of other andesitic stratovolcanoes. The historical activity of the Soufrière Hills volcano on Montserrat Island in the Lesser Antilles (Cole et al., 2014) represents a well-documented case for comparison with Pico de Orizaba's eruptive behavior. During the Xilomich eruptive episode (8890–8170 yr BP), Pico de Orizaba experienced at least two dome collapses and four Vulcanian-type eruptions, which produced scoria-and-ash pyroclastic flows, alternating with phases of Plinian-subplinian activity, including the Xil-fall pyroclastic fall (Cítaltepétl Pumice Layers E-F; Rossotti and Nuñez, 2004). A similar eruptive pattern has been observed at the Soufrière Hills volcano, which over the past 30 years has experienced more than a hundred Vulcanian explosions and dome collapses (Cole et al., 2014). Dome failures at Soufrière Hills frequently trigger explosive activity, producing tephra plumes that rise over 5 km in height and generating pyroclastic density currents. Notably, during the 1997 eruptive episode, Soufrière Hills produced both dilute and dense pyroclastic density currents interbedded with lapilli scoria fallout, illustrating an eruptive dynamic comparable to the behavior inferred for the Xilomich eruptive episode.

### 8.3. Hazards implications

Our results indicate that the Pico de Orizaba volcano was very active during the Xilomich eruptive episode (8980–8170 yr BP). During this time (ca. 810 years), the volcano emplaced more than 31 m of pyroclastic flow deposits on its southern flank. Five eruptions (A–E) produced the Xil-1 to Xil-5 pyroclastic flow deposits between 8980 and 8660 yr BP (ca. 320 years). Probably, Xil-5 to Xil-9 units were produced by a single eruption (E), and the last eruptive event (F) took place some 8170 yr BP with the emplacement of the Xil-10 block-and-ash flow (Höskuldsson and Robin, 1993).

The smooth topography of the southern plain of Pico de Orizaba (Fig. 10) suggests that Xilomich flow deposits partly filled the ravines made with older lavas of the volcano and the underlying Cretaceous limestones and shales of the local substrate (Yáñez and García, 1982). The modern towns of Texmalaquilla, Loma Grande, Texmola, and Esperanza, inhabited by 25,820 people (National Institute of Statistics and Geography (INEGI), 2020a–c), are settled upon these pyroclastic and subsequent volcaniclastic deposits. The present morphology of the southern flanks of the volcano progressively decreases in elevation between Texmola, Loma Grande, Plan del Capulín, and San José Síchil (Fig. 10). Therefore, future activity of the volcano could endanger these communities that may be especially vulnerable to pyroclastic flow activity. These types of hazards easily follow the natural topographic gradient downstream and may directly threaten inhabited areas. Such a scenario is possible as supporting evidence provided by the presence of a pyroclastic flow deposit dated at 8980 yr BP in the Maltrata and Ciudad Mendoza region (Höskuldsson and Robin, 1993; Carrasco-Núñez and Rose, 1995). This deposit provides compelling evidence that pyroclastic flows from the Xilomich eruptive episode reached as far as Maltrata, Ciudad Mendoza, Nogales, Río Blanco, and Orizaba, located within a 20–30 km radius south of Pico de Orizaba (Fig. 10). These towns are inhabited by approximately 284,664 people (INEGI, 2020) and have been founded within a valley that make them particularly vulnerable to future pyroclastic flows. Settlements located on adjacent topographic highs are not exempt from hazard, as they may be affected by ash clouds that decouple from the main pyroclastic flow body and may flow laterally over ridges and elevated landforms.

Because the current hazard map for Pico de Orizaba was created in 2001 using incomplete data, the development of an updated volcanic hazard map is essential to enhance risk mitigation strategies and strengthen the resilience of communities around Pico de Orizaba.

## 9. Concluding remarks

- Descriptions and correlations of the pyroclastic deposits south of Pico de Orizaba, supported by grain-size and component analyses, petrography of the juvenile clasts, and five new radiocarbon dates, have enabled a comprehensive reconstruction of the Xilomich pyroclastic sequence deposited south of Pico de Orizaba between 8980 and 8170 yr BP.
- Ten pyroclastic flow deposits were recognized: four scoria-and-ash (Xil-1, Xil-3, Xil-5, Xil-6), one pumice-and-ash (Xil-2), two block-and-ash (Xil-4 and Xil-10), and three undifferentiated deposits (Xil-7 to Xil-9).
- Pico de Orizaba experienced repeated Vulcanian activity (at least four times) and dome-collapse producing scoria-and-ash and block-and-ash flows during the Xilomich episode.
- More than 31 m of pyroclastic flow deposits, interlayered with paleosol, layers containing horizontally oriented burned grass and tree twigs, and reworked deposits associated with the Xilomich eruptive episode, were measured in a distance of 12.5 km from the volcano.
- About 310,500 people live within a 30 km radius south of Pico de Orizaba, where pyroclastic flows were deposited over the last 8980 years BP.

## CRediT authorship contribution statement

**Delphine Sourisseau:** Writing – review & editing, Writing – original draft, Visualization, Methodology, Investigation, Formal analysis, Conceptualization. **José Luis Arce:** Writing – review & editing, Supervision, Investigation, Funding acquisition, Conceptualization. **José Luis Macías:** Writing – review & editing, Funding acquisition. **Laura E. Beramendi-Orosco:** Formal analysis, Writing – review & editing. **José Juan Carrillo-Mondragón:** Investigation. **Galia Gonzalez-Hernandez:** Formal analysis, Writing – review & editing.

## Declaration of competing interest

The authors declare that they have no known competing financial interests or personal relationships that could have appeared to influence the work reported in this paper.

## Acknowledgments

This work was supported by a Secretaría de Ciencia, Humanidades, Tecnología e Innovación (SECIHTI) Postdoctoral Grant awarded to the first author. The analyses were funded by the DGAPA-UNAM Programa de Apoyo a Proyectos de Investigación e Innovación Tecnológica (PAPIIT) Grant IN101123 awarded to José Luis Arce and Grant IN119523 to José Luis Macías. We are grateful to Consuelo Macías Romo for her assistance with sample preparation. We would like to express our gratitude to Jaime Díaz-Ortega and Silvia Martínez-Cruz for the elaboration of thin sections. We also extend our thanks to Fabiola Mendiola for her technical support in the Fine Particulate Laboratory at the Geophysics Institute Michoacán Unit (IGUM)-UNAM. We thank Guillermo Cisneros Máximo for his help with the ArcGIS software (IGUM-UNAM). I would like to thank Ariadna Guadalupe Ramírez for her help with the population distribution around Pico de Orizaba. Special thanks to the entire Geology Institute for their support and assistance in conducting this work. Two anonymous reviewers made valuable comments to improve the final version of the manuscript.

## Appendix A. Supplementary data

Supplementary data to this article can be found online at <https://doi.org/10.1016/j.jvolgeores.2025.108433>.

## Data availability

Data is available in the Supplementary Material Excel spreadsheet, Tables 1, 2, 3, 4, 5, 6, and 7.

## References

- Beramendi-Oroasco, L.E., Gonzalez-Hernandez, G., Urrutia-Fucugauchi, J., Morton-Bermea, O., 2006. Radiocarbon Laboratory at the National Autonomous University of Mexico: first set of samples and new 14C internal reference material. *Radiocarbon* 48 (3), 485–491. <https://doi.org/10.1017/S0033822200038911>.
- Bronk Ramsey, C., 2021. Oxcal v4. 4.4 Calibration Program. Website. <https://c14.arch.ox.ac.uk/oxcal/OxCal.html>.
- Calder, E.S., Sparks, R.S.J., Gardeweg, M.C., 2000. Erosion, transport and segregation of pumice and lithic clasts in pyroclastic flows inferred from ignimbrite at Lascar Volcano, Chile. *J. Volcanol. Geotherm. Res.* 104 (1–4), 201–235. [https://doi.org/10.1016/S0377-0273\(00\)00207-9](https://doi.org/10.1016/S0377-0273(00)00207-9).
- Cantagrel, J.M., Robin, C., 1979. K-Ar dating on eastern Mexican volcanic rocks—relations between the andesitic and the alkaline provinces. *J. Volcanol. Geotherm. Res.* 5 (1–2), 99–114. [https://doi.org/10.1016/0377-0273\(79\)90035-0](https://doi.org/10.1016/0377-0273(79)90035-0).
- Cantagrel, J.M., Gourgaud, A., Robin, C., 1984. Repetitive mixing events and Holocene pyroclastic activity at Pico de Orizaba and Popocatepetl (Mexico). *Bull. Volcanol.* 47, 735–748. <https://doi.org/10.1007/BF01952341>.
- Carrasco-Núñez, G., 2000. Structure and Proximal Stratigraphy of Citlaltépetl Volcano (Pico de Orizaba), Mexico.
- Carrasco-Núñez, G., Rose, W.I., 1995. Eruption of a major Holocene pyroclastic flow at Citlaltépetl volcano (Pico de Orizaba), México, 8.5–9.0 ka. *J. Volcanol. Geotherm. Res.* 69 (3–4), 197–215. [https://doi.org/10.1016/0377-0273\(95\)00023-2](https://doi.org/10.1016/0377-0273(95)00023-2).
- Carrasco-Núñez, G., Vallance, J.W., Rose, W.I., 1993. A voluminous avalanche-induced lahar from Citlaltépetl volcano, Mexico: implications for hazard assessment. *J. Volcanol. Geotherm. Res.* 59 (1–2), 35–46. [https://doi.org/10.1016/0377-0273\(93\)90076-4](https://doi.org/10.1016/0377-0273(93)90076-4).
- Carrasco-Núñez, G., Díaz-Castellón, R., Siebert, L., Hubbard, B., Sheridan, M.F., Rodríguez, S.R., 2006. Multiple edifice-collapse events in the Eastern Mexican Volcanic Belt: the role of sloping substrate and implications for hazard assessment. *J. Volcanol. Geotherm. Res.* 158 (1–2), 151–176. <https://doi.org/10.1016/j.jvolgeores.2006.04.025>.
- Carrasco-Núñez, G., Siebert, L., Díaz-Castellón, R., Vázquez-Sellem, L., Capra, L., 2010. Evolution and hazards of a long-quiescent compound shield-like volcano: Cofre de Perote, Eastern Trans-Mexican Volcanic Belt. *J. Volcanol. Geotherm. Res.* 197 (1–4), 209–224. <https://doi.org/10.1016/j.jvolgeores.2009.08.010>.
- Carrasco-Núñez, G., Bernal, J.P., Dávila, P., Jicha, B., Giordano, G., Hernández, J., 2018. Reappraisal of Los Humeros volcanic complex by new U/Th zircon and 40Ar/39Ar dating: Implications for greater geothermal potential. *Geochem. Geophys. Geosyst.* 19 (1), 132–149. <https://doi.org/10.1002/2017GC007044>.
- Carrasco-Núñez, G., Hernández, J., Cavazos-Álvarez, J., Norini, G., Orozco-Esquível, T., López-Quiroz, P., De León-Barragán, L., 2021. Volcanic geology of the easternmost sector of the Trans-Mexican Volcanic Belt, Mexico. *J. Maps* 17 (2), 486–496. <https://doi.org/10.1080/17445647.2021.1970037>.
- Cashman, K.V., Sparks, R.S.J., 2013. How volcanoes work: a 25 year perspective. *Bulletin* 125 (5–6), 664–690. <https://doi.org/10.1130/B30720.1>.
- Cavazos-Alvarez, J.A., Carrasco-Núñez, G., Sosa-Ceballos, G., Lucci, F., 2024. Evolution of a large Quaternary monogenetic field; the multifaceted volcanism of the Serdán-oriental basin, México. *J. Volcanol. Geotherm. Res.* 446, 107999. <https://doi.org/10.1016/j.jvolgeores.2023.107999>.
- Clarke, A.B., Voight, B., Neri, A., Macedonio, G., 2002. Transient dynamics of vulcanian explosions and column collapse. *Nature* 415 (6874), 897–901. <https://doi.org/10.1038/415897a>.
- Cole, P.D., Calder, E.S., Sparks, R.S.J., Clarke, A.B., Druitt, T.H., Young, S.R., Norton, G. E., 2002. Deposits from dome-collapse and fountain-collapse pyroclastic flows at Soufrière Hills Volcano, Montserrat. <https://doi.org/10.1144/GSL-MEM.2002.021.01.11>.
- Cole, P.D., Smith, P.J., Stinton, A.J., Odbert, H.M., Bernstein, M.L., Komorowski, J.C., Stewart, R., 2014. Vulcanian Explosions at Soufrière Hills Volcano, Montserrat between 2008 and 2010. <https://doi.org/10.1144/M39.5>.
- Cole, P.D., Barclay, J., Robertson, R.E.A., Mitchell, S., Davies, B.V., Constantinescu, R., Stinton, A., 2024. Explosive sequence of La Soufrière, St Vincent, April 2021: insights into drivers and consequences via eruptive products. *Geol. Soc. Lond. Spec. Publ.* 539 (1), 81–106. <https://doi.org/10.1144/SP539-2022-292>.
- DeMets, C., Stein, S., 1990. Present-day kinematics of the Rivera plate and implications for tectonics in southwestern Mexico. *J. Geophys. Res. Solid Earth* 95 (B13), 21931–21948. <https://doi.org/10.1029/B13p21931>.
- Druitt, T.H., Young, S.R., Baptie, B., Bonadonna, C., Calder, E.S., Clarke, A.B., Voight, B., 2002. Episodes of cyclic Vulcanian explosive activity with fountain collapse at Soufrière Hills Volcano, Montserrat. <https://doi.org/10.1144/GSL-MEM.2002.021.01.13>.
- Ferrari, L., Orozco-Esquível, T., Manea, V., Manea, M., 2012. The dynamic history of the Trans-Mexican Volcanic Belt and the Mexico subduction zone. *Tectonophysics* 522, 122–149. <https://doi.org/10.1016/j.tecto.2011.09.018>.
- Gómez-Vazquez, A., De la Cruz-Reyna, S., Mendoza-Rosas, A.T., 2016. The ongoing dome emplacement and destruction cyclic process at Popocatépetl volcano, Central Mexico. *Bull. Volcanol.* 78, 1–15. <https://doi.org/10.1007/s00445-016-1054-z>.
- Höskuldsson, A., 1992. Le complexe volcanique Pico de Orizaba, Sierra Negra-Cerro Las Cumbres (Sud-Est mexicain): structure, dynamismes éruptifs et évaluations des aléas (Doctoral dissertation, Clermont-Ferrand 2).
- Höskuldsson, A., Robin, C., 1993. Late Pleistocene to Holocene eruptive activity of Pico de Orizaba, eastern Mexico. *Bull. Volcanol.* 55, 571–587. <https://doi.org/10.1007/BF00301810>.
- Inman, D.L., 1952. Measures for describing the size distribution of sediments. *J. Sediment. Res.* 22 (3), 125–145. <https://doi.org/10.1306/D42694DB-2B26-11D7-8648000102C1865D>.
- Kelfoun, K., Santos, A.B., Latchimy, T., Bontemps, M., Nurdien, I., Beauducel, F., Gueugneau, V., 2021. Growth and collapse of the 2018–2019 lava dome of Merapi volcano. *Bull. Volcanol.* 83, 1–13. <https://doi.org/10.1007/s00445-020-01428-x>.
- Macías, J.L., Arce, J.L., García-Tenorio, F., Sosa-Ceballos, G., Gardner, J.E., 2020. Source and behavior of pyroclastic density currents generated by Vulcanian-style explosions of Popocatépetl volcano (Mexico) on 22 January 2001. *J. Volcanol. Geotherm. Res.* 406, 107071. <https://doi.org/10.1016/j.jvolgeores.2020.107071>.
- Mooser, F., Maldonado Koerell, M., 1961. Penecontemporaneous tectonics along the Mexican Pacific coast. *Geofis. Int.* 1, 1–20.
- Nakada, S., Fujii, T., 1993. Preliminary report on the activity at Unzen Volcano (Japan), November 1990–November 1991: Dacite lava domes and pyroclastic flows. *J. Volcanol. Geotherm. Res.* 54 (3–4), 319–333. [https://doi.org/10.1016/0377-0273\(93\)90070-8](https://doi.org/10.1016/0377-0273(93)90070-8).
- National Institute of Statistics and Geography (INEGI), 2020a. Main results by AGEB and urban block 2020. Consultation date: January 22, 2025. <https://www.inegi.org.mx/app/scitel/Default?ev=10>.
- National Institute of Statistics and Geography (INEGI), 2020b. Main results by locality (ITER) 2020. Consultation date: January 20, 2025. <https://www.inegi.org.mx/app/scitel/Default?ev=9>.
- National Institute of Statistics and Geography (INEGI), 2020c. Geostatistical Framework (MG). Consultation date: January 20, 2025. [https://www.inegi.org.mx/prog\\_ramas/mg/](https://www.inegi.org.mx/prog_ramas/mg/).
- Nixon, G.T., 1982. The relationship between Quaternary volcanism in Central Mexico and the seismicity and structure of subducted ocean lithosphere. *Geol. Soc. Am. Bull.* 93 (6), 514–523. [https://doi.org/10.1130/0016-7606\(1982\)93<514:TRBVVI>2.0.CO;2](https://doi.org/10.1130/0016-7606(1982)93<514:TRBVVI>2.0.CO;2).
- Pardo, M., Suárez, G., 1995. Shape of the subducted Rivera and Cocos plates in southern Mexico: seismic and tectonic implications. *J. Geophys. Res. Solid Earth* 100 (B7), 12357–12373. <https://doi.org/10.1029/95JB00919>.
- Reimer, P.J., Austin, W.E., Bard, E., Bayliss, A., Blackwell, P.G., Ramsey, C.B., Talamo, S., 2020. The IntCal20 Northern Hemisphere radiocarbon age calibration curve (0–55 cal kBP). *Radiocarbon* 62 (4), 725–757. <https://doi.org/10.1017/RDC.2020.41>.
- Robin, C., Cantagrel, J.M., 1982. Le Pico de Orizaba (Mexique): structure et évolution d'un grand volcan andésitique complexe. *Bull. Volcanol.* 45, 299–315. <https://doi.org/10.1007/BF02597254>.
- Rodríguez, S.R., 2005. Geology of Las Cumbres Volcanic Complex, Puebla and Veracruz states, Mexico. *Rev. Mex. Cienc. Geol.* 22 (2), 181–198.
- Rossotti, A., Núñez, G.C., 2004. Stratigraphy of the 8.5 9.0 ka BP Citlaltépetl pumice fallout sequence. *Rev. Mex. Cienc. Geol.* 21 (3), 353–370.
- Rossotti, A., Carrasco-Núñez, G., Rosi, M., Di Muro, A., 2006. Eruptive dynamics of the “Citlaltépetl pumice” at Citlaltépetl volcano, eastern Mexico. *J. Volcanol. Geotherm. Res.* 158 (3–4), 401–429. <https://doi.org/10.1016/j.jvolgeores.2006.07.008>.
- Saucedo, R., Macías, J.L., Gavilanes, J.C., Arce, J.L., Komorowski, J.C., Gardner, J.E., Valdez-Moreno, G., 2010. Eyewitness, stratigraphy, chemistry, and eruptive dynamics of the 1913 Plinian eruption of Volcán de Colima, México. *Journal of volcanology and geothermal research* 191 (3–4), 149–166. <https://doi.org/10.1016/j.jvolgeores.2010.01.011>.
- Saucedo, R., Macías, J.L., Sheridan, M.F., Bursik, M.I., Komorowski, J.C., 2005. Modeling of pyroclastic flows of Colima Volcano, Mexico: implications for hazard assessment. *J. Volcanol. Geotherm. Res.* 139 (1–2), 103–115. <https://doi.org/10.1016/j.jvolgeores.2004.06.019>.
- Siebe, C., Abrams, M., Sheridan, M.F., 1993. Major Holocene block-and-ash fan at the western slope of ice-capped Pico de Orizaba volcano, México: Implications for future hazards. *J. Volcanol. Geotherm. Res.* 59 (1–2), 1–33. [https://doi.org/10.1016/0377-0273\(93\)90075-3](https://doi.org/10.1016/0377-0273(93)90075-3).
- Sohn, Y.K., Chough, S.K., 1989. Depositional processes of the Suwolbong tuff ring, Cheju Island (Korea). *Sedimentology* 36 (5), 837–855. <https://doi.org/10.1111/j.1365-3091.1989.tb01749.x>.
- Targulian, V.O., Krasilnikov, P.V., 2007. Soil system and pedogenic processes: Self-organization, time scales, and environmental significance. *Catena* 71 (3), 373–381. <https://doi.org/10.1016/j.catena.2007.03.007>.
- Varley, N.R., Arámbula-Mendoza, R., Reyes-Dávila, G., Stevenson, J., Harwood, R., 2010. Long-period seismicity during magma movement at Volcán de Colima. *Bull. Volcanol.* 72, 1093–1107. <https://doi.org/10.1007/s00445-010-0390-7>.
- Vásquez-Montoya, M., Torres-Orozco, R., Arce, J.L., Sieron, K., Córdoba-Montiel, F., 2025. Unraveling recurrent Pleistocene-Holocene multiphase explosive eruptions of Pico de Orizaba (Citlaltépetl), Mexico, from lithostratigraphic analysis and radiocarbon dating. *J. Volcanol. Geotherm. Res.* 108384. <https://doi.org/10.1016/j.jvolgeores.2025.108384>.
- Yamamoto, T., Takarada, S., Suto, S., 1993. Pyroclastic flows from the 1991 eruption of Unzen volcano, Japan. *Bull. Volcanol.* 55, 166–175. <https://doi.org/10.1007/BF00301514>.
- Yáñez, C., García, S., 1982. Exploración de la región geotérmica Los Humeros-Las Derrumbadas, Estados de Puebla y Veracruz (Internal report, Comisión Federal de Electricidad, Mexico City, pp. 1–96.